U.PORTO
FACULDADE DE CIÊNCIAS
UNIVERSIDADE DO PORTO

MSc

Microstructured Optical Fibers for Fluid Sensing Applications

João Pedro Pinto Moura

Master's Dissertation submitted to the
Faculty of Sciences of the University of Porto in
Engineering Physics

2014

MSc
2nd CYCLE
FCUP
2014
U.PORTO
Microstructured Optical Fibers for Fluid Sensing Applications
João Pedro Pinto Moura
FC

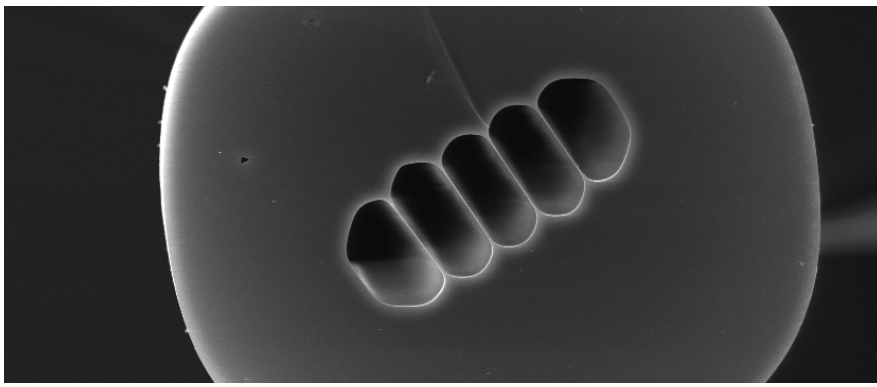

Microstructured Optical Fibers for Fluid Sensing Applications

João Pedro Pinto Moura
Integrated Master's in Engineering Physics
Department of Physics
2014

Supervisor
Orlando José dos Reis Frazão, Invited Assistant Professor, Faculty of Sciences of the University of Porto

Co-Supervisor
José Luís Campos de Oliveira Santos, Full Professor, Faculty of Sciences of the University of Porto

All modifications determined by the Jury, and only those, were made.

The president of the Jury:

Porto, _____/_____/_____

Acknowledgements

Life is an inherently social experience. It is a collaborative process comprised of accumulated experiences to which several individuals contribute to. Thus arises the relevance of acknowledging those who were most relevant in my personal and professional development, and who are ultimately responsible for providing me with all the necessary tools to accomplish this dissertation:

- Dr. Orlando Frazão, who patiently and supportively accompanied me throughout this entire endeavor, and whose experimental proficiency and creativity at times seemed almost like magic;

- Prof. José Luís Santos, whose detailed reviews and critical comments provided crucial insights to this dissertation;

- The whole staff of the Centre for Applied Photonics of INESC TEC, who embraced me as a part of their team and allowed me to participate in conferences nationally and abroad;

- Marta Ferreira and Susana Silva, who were always available whenever my experimental or theoretical skills were lacking;

- Prof. Manuel Joaquim Marques and Prof. António Pereira Leite, whose theoretical understanding of Optics allowed for profitable discussions;

- The Optical Fiber Technology group of IPHT in Jena, Germany, particularly Jens Kobelke, Jörg Bierlich, Katrin Wondraczek and Kay Schuster, who warmly received and taught me during the month of March 2014 as a part of their research team, and whose experience in fiber drawing was invaluable;

- Ricardo André, who made me feel at home during my time in Jena and was a fundamental contributor to the fiber post-processing using Focused Ion Beam;

- The Portuguese and German governments, which through FCT and DAAD, respectively, financed my stay in Jena;

- Mafalda Monteiro, Tiago Lima, Diogo Lopes, José Valente, Artur Amorim and Daniel Passos, my university colleagues who went through the same struggles as I and finally became close personal friends;

- A minha mãe, pai, irmã e restante família que sempre me proporcionaram uma vida confortável e feliz, que contínua e inequivocamente contribuíram para a minha educação e que influenciaram em grande parte a minha personalidade, definindo categoricamente a pessoa que hoje sou;

- Ana Santos, Ana Dias, Ana Bernardino and, especially, Flávio Fonseca, the "family I chose with my heart" whose unconditional care and support I will keep on cherishing forever.

To all those here mentioned, my deepest appreciation.

Resumo

Os sensores em fibra óptica são uma das áreas de investigação mais proeminentes no domínio da fibra óptica. Este campo foi fortemente estimulado com o aparecimento das Fibras Ópticas Microestruturadas (MOFs) que possibilitam o controlo estrutural de fibras a uma escala muito pequena. Em particular, MOFs com alvéolos que permitem a interacção de luz com fluídos são elementos promissores em novos esquemas de detecção. Esta dissertação abrange o fabrico, pós-processamento e aplicação de MOFs em sensores de fluídos.

Após uma breve revisão dos sensores químicos em fibra óptica, é descrito o processo de desenho e fabrico de uma MOF com cinco alvéolos, assemelhando-se estruturalmente a "uma lagarta", através de um processo de empilhamento e estiramento, com a intenção da sua aplicação em sensores de fluídos. Esta fibra foi seguidamente pós-processada usando um feixe de iões focado para a criação de canais microfluídicos que permitem a entrada de fluídos do exterior para o interior da fibra mesmo que os seus extremos sejam fechados.

Posteriormente, uma fibra de núcleo suspenso fundida com uma fibra monomodo resultou na proposta de uma nova configuração para um sensor de compostos orgânicos voláteis. Enchendo os alvéolos da fibra com estes compostos na fase líquida através de forças de capilaridade e observando a dinâmica do processo de evaporação foi possível diferenciar o comportamento de acetona e de álcool isopropílico, abrindo as portas para uma nova classe de sensores baseados na monitorização de fenómenos de evaporação.

No final são apresentadas propostas de futuros desenvolvimentos baseados no que foi concretizado com esta dissertação, evidenciando o potencial que este trabalho poderá ter na área dos sensores em fibra óptica.

Palavras-Chave: fibras ópticas microestruturadas, sensores em fibra óptica, estiramento de fibras, feixe de iões focado, pós-processamento de fibras, compostos orgânicos voláteis, sensores de fluídos.

Abstract

Optical fiber sensors are one of today's most prominent research fields in the optical fibers's domain. This area has been greatly stimulated by the appearance of Microstructured Optical Fibers (MOFs) which allow the structural tailoring of fibers at a very small scale. In particular, MOFs with holes that allow the interaction of fluids with light hold promises in new detection configurations. The present dissertation addresses the fabrication, post-processing and application of MOFs in fluid sensing.

After a brief review on chemical optical fiber sensing, the design and fabrication of a five-hole caterpillar-like MOF through a stack-and-draw procedure is described, envisaging future applications in fluid sensing. This fiber was subsequently post-processed using a Focused Ion Beam in order to create microfluidic channels to the external environment that would allow fluids to flow in and out of the fiber even after being spliced on both ends.

Afterwards, a suspended-core fiber was fusion spliced to a single-mode fiber and a new sensing configuration was proposed for the detection of volatile organic compounds. By allowing these substances to fill the fiber's holes in the liquid phase through capillarity forces and then tracking their evaporation dynamics, it was possible to distinguish the behaviour of acetone and isopropyl alcohol, paving the way to a new class of sensors based on evaporation monitoring.

Finally, proposals on future developments based on what was achieved with this dissertation are mentioned, evidencing the potential that this work may have in the area of optical fiber sensing.

Keywords: microstructured optical fibers, optical fiber sensors, fiber drawing, focused ion beam, fiber post-processing, volatile organic compounds, fluid sensing.

Index

List of Figures

List of Tables

Nomenclature

FBG	Fiber Bragg Grating
FIB	Focused Ion Beam
FSR	Free Spectral Range
$\boldsymbol{L}$	Length
MOF	Microstructured Optical Fiber
OSA	Optical Spectrum Analyser
OTDR	Optical Time-Domain Reflectometry
PCF	Photonic Crystal Fiber
PF	Hole Power Fraction
$\boldsymbol{R}$	Reflection Coefficient
RI, $\boldsymbol{n}$	Refractive Index
SCF	Suspended Core Fiber
SEM	Scanning Electron Microscopy
SMF	Single Mode Fiber
SPR	Surface Plasmon Resonance
TIR	Total Internal Reflection
$\boldsymbol{\lambda}$	Wavelength
VOC	Volatile Organic Compound
WDM	Wavelength Division Multiplexing

Chapter 1

Introduction

1.1 Motivation

Until the 1970s, telecommunications were limited by the then used coaxial cable microwave technology, both in terms of slow bit-rates and short lengths for signal repeaters [1]. In 1966, Charles Kao and George Hockman laid the theoretical foundations of optical fiber waveguides [2] which, together with the discovery of the laser in the 1960s as a coherent light source, would soon revolutionize telecommunications. Kao's crucial contribution was later recognised with the 2009 Nobel Prize in Physics "*for groundbreaking achievements concerning the transmission of light in fibers for optical communication*" [3].

Optical fibers were indeed one of the most important technological achievements of the XX century. A description of the evolution of optical fibers for communication systems can be found in the literature [1]. Since the 1970s, this technology has been further developed due to society's need to continuously improve the efficiency of telecommunications. This lead to today's modern systems that use: low loss, dispersion-shifted *single mode fibers* (SMFs), with attenuation coefficients as small as $0.2\,\mathrm{dB\,km^{-1}}$, which extend the required signal repeater length above 100 km; all-optical signal amplification schemes, which eliminate the need for slow optoelectronic conversion circuits; and *wavelength-division multiplexing* (WDM), which allows the simultaneous usage of several wavelengths for information transmission. Present-day technology works with bit-rate–length products[1] of over $10\,\mathrm{Pb\,s^{-1}\cdot km}$, 8 orders of magnitude above those of microwave coaxial cables. To-

[1] A figure of merit to compare communication systems which consists on the product of bit-rate with the required length between signal repeaters.

day, optical fiber technology powers all kinds of ground-level communication systems, from intercontinental information transmission to distribution of media contents at the individual house level.

That said, considering the massive economic relevance of telecommunications, it is understandable that fiber optics is one of today's most prominent research areas. Through a spillover effect, this led to other applications such as fiber lasers, supercontinuum light sources, particle scintillators, and, notably, fiber sensors [4]. Optical fiber sensors are built on this large bandwidth multiplexed technology with numerous advantages in comparison with conventional electronic sensing setups and several review papers about fiber sensing technology can be found in the literature [4, 5]. Fiber sensors are lightweight, small and immune to electromagnetic interference. The transduction process is performed by the interaction of light that propagates within a fiber with the external environment. Depending on the type of interaction, several properties of light can be altered, such as intensity, wavelength, phase or polarization. These properties can be translated into measurements of multiple physical parameters such as strain, curvature, temperature, pressure, torsion, magnetic field, or refractive index, as well as chemical and biological properties. Due to these factors, optical fiber sensors have already developed into a market of their own, with a 2012 global market size of 1.5 billion USD and estimated annual growth rates ranging between 10% and 20% until 2017 [6, 7].

Several different sensing elements and setups have been used in optical fiber sensing. One can remotely measure light that is reflected or transmitted from a fiber sensor, and in some cases a single fiber can be used to measure properties along its length, either continuously, by measuring intrinsic scattering effects with Optical Time-Domain Reflectometry (OTDR), or discretely, using WDM to obtain information from several sensors by restricting interactions in a specific sensing element with predefined wavelengths, for example. In addition, different sensing elements are characterised by the process through which light interacts with measurands. Some notable sensing elements are Fiber Bragg Gratings (FBGs), Long Period Gratings (LPGs), Quantum Dots, Tapers or Plasmonic Coatings.

Moreover, the need for tailoring specific fiber properties such as dispersion and birefringence resulted in the unprecedented ability to create a large variety of fiber designs at an even smaller scale – the so called *Microstructured Optical Fibers* (MOFs). In par-

ticular, one can create a wide diversity of microstructured fibers with holes to allow the inflow of fluids and maximize their interaction with light propagating inside the fiber. This approach holds promises in high sensitivity sensing applications such as industrial or environmental process monitoring or biochemical analysis. This dissertation focuses on the exploration of MOFs for fluid sensing applications.

1.2 Aim and Objectives

The aim of this dissertation is to cover a wide range of aspects related with MOFs for fluid sensing, from their fabrication to the actual implementation in a particular sensing configuration. To accomplish this, the following objectives were defined:

- Fabrication of an MOF with large holes for easier filling with fluids;
- Manufacture of MOF-based sensing heads;
- Post-processing of the MOFs for the creation of microfluidic channels to allow the infiltration of fluids;
- Study of sensing configurations for the identification of Volatile Organic Compounds.

1.3 Structure

This document starts with an overview on chemical optical fiber sensing. The most common sensing configurations and principles are described as well as the relevance that MOFs have in this regard. Additionally, the importance of interferometry is revealed, with this being one of the main tools that can be exploited in optical sensing.

Following this overview, the fabrication and post-processing of an MOF with a structure which resembles that of a caterpillar is presented. Targeting the manufacture of interferometric fluid sensors, this fiber is comprised of five large holes separated by submicrometric walls and was fabricated through a stack-and-draw procedure. After drawing, several fiber samples were post-processed using a Focused Ion Beam in order to create microfluidic channels that allow fluid flow even after splicing to other standard fibers. The results of both the fabrication and post-processing steps are detailed.

Afterwards, special attention is given to Volatile Organic Compound sensing. The relevance of these substances is presented, as well as a review on their detection with optical sensors. Subsequently, the large holes of a Suspended-Core Fiber are filled with volatile compounds and their evaporation dynamics are tracked. This methodology is used to distinguish between two compounds according to differences in their respective dynamics.

Finally, after summing up the information presented, a list of potential further developments is given.

1.4 Outputs

The work developed throughout this dissertation was communicated to the scientific community through the publication of a paper in a scientific journal of reference and through oral and poster presentations in three conferences, as listed below:

- J. P. Moura, H. Baierl, J.-L. Auguste, R. Jamier, P. Roy, J. L. Santos, and O. Frazão, *Evaporation of volatile compounds in suspended-core fibers*, Optics Letters, vol. 39, no. 15, 2014;
- J. P. Moura, H. Baierl, J.-L. Auguste, R. Jamier, P. Roy, J. L. Santos, and O. Frazão, *Fluid evaporation monitoring with suspended-core fibers*, II International Conference on Applications of Optics and Photonics, 26-30 May 2014, Aveiro, Portugal;
- J. P. Moura, H. Baierl, J.-L. Auguste, R. Jamier, P. Roy, J. L. Santos, and O. Frazão, *Evaporation of fluids in suspended-core fibers*, Third Mediterranean Photonics Conference, 7-9 May 2014, Trani, Italy;
- J. P. Moura, J. L. Santos, and O. Frazão, *Evaporation of fluids in microstructured fibers*, IJUP'14 – 7th Meeting of Junior Researchers from the University of Porto, 13 Feb 2014, Porto;
- J. P. Moura, J. L. Santos, and O. Frazão, *Evaporação de Compostos Voláteis em Fibras de Núcleo Suspenso*, FÍSICA 2014 – 19ª Conferência Nacional de Física, 2-4 Sep 2014, Lisboa.

Chapter 2

Chemical Optical Fiber Sensing

2.1 Introduction

Chemical sensing is a crucial step in diverse applications such as the monitoring of environmental parameters, quality control in industrial processes or the identification of biochemical elements in medical analysis. The potential that optical fiber sensors have in this regard has led to strong research efforts in this area. In this chapter, a short review on chemical sensing of gases and liquids using optical fibers is presented, contextualizing the work that was carried.

In most optical fiber sensors for fluid sensing, a gas or liquid is detected by enabling its interaction with light. This can be performed using a variety of sensing principles and configurations. One of the earliest chemical sensors is the *optrode*, depicted in fig. 2.1, where the analyte modifies the optical properties of a reacting material which is probed by a single mode optical fiber (SMF) [5, 8, 9]. Optical properties such as reflectance, absorbance, fluorescence or chemiluminescence can be measured in reflection or transmission geometries to identify the presence of the analyte to which the reagent phase reacts to [4]. Notwithstanding its simple geometry, the optrode is still the object of extensive research since specific sensors can be created just by altering the chemical/biochemical properties of the reagent phase [10].

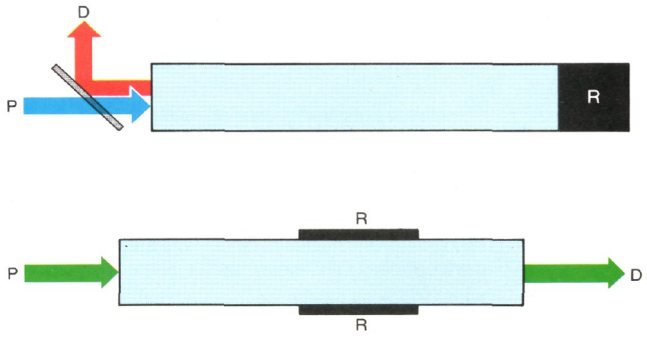

Figure 2.1: An *optrode* has a reagent phase (R) that reacts with the analyte. A probe beam (P) interacts with the reagent phase and is detected (D) afterwards. Two possible geometry variations are shown: reflection (top) and transmission (bottom). Figure reproduced from [9].

2.2 Microstructured Fibers in Chemical Sensing

Independent of the sensing configuration, the higher the interaction between light and the analyte, the better the sensor performance will be. In general, by increasing the overlap of guided modes with the analyte, a sensor's sensitivity is increased [11].

One can then conclude that microstructured optical fibers (MOFs) have a great potential for biochemical optical fiber sensing since they allow great design flexibility. Fluids can be placed inside the holes of MOFs where light propagates either mostly inside a large central hole (Photonic Bandgap Fibers) or evanescently inside the smaller holes that compose the cladding through Total Internal Reflection (TIR). Thus, by appropriately calibrating parameters related to the overall structure, like core diameter, refractive index of glass, diameter of air holes, pitch and the cross-section lattice structure, it is possible to increase the *hole power fraction*[1] [12]. Furthermore, since MOFs are in general composed only of silica glass, their temperature sensitivity is inherently small, thus reducing cross-sensitivity between temperature and the measurand [13]. A more detailed review on the origin and fabrication of MOFs will be presented in chapter 3.

Regarding hole power fraction maximization, photonic bandgap fibers would in principle be better suited for chemical sensing since propagation happens almost entirely inside the hollow-core region (with hole power fractions that can be higher than 95 %) [14]. However, TIR MOFs are easier to fabricate and splice to SMFs [11, 15]. Thus, TIR MOFs are often still preferred over photonic bandgap fibers, even though the former have much

[1]The evanescent or hole power fraction can be defined as the evanescent power flux that propagates within the holes of a MOF or in other air-filled regions, divided by the fiber's total power flux.

lower power fractions inside air holes, requiring higher fiber lengths to attain the same equivalent free-space interaction length[2]. Nonetheless, by correctly designing the cross-section of a TIR MOF one can obtain hole power fractions high enough to allow their usage in practical applications [16].

The interaction between the evanescent field in microstructured fiber holes and fluids has been the object of extensive study for sensing purposes which translates in a high number of published reviews [11, 12, 15, 17, 18]. These report the large variety of setups used in fluid sensing with MOFs which can either be based on surface functionalization with a reagent phase for increased specificity, or label-free measurements of refractive index or absorption spectrum.

MOFs can be filled with fluids simply by placing the fiber in an environment with the liquid or gas that one intends to measure. If both ends of the MOF are open, capillarity forces are in general sufficient for complete filling of the MOF. However, in the case of liquids, if one end of the MOF is closed, capillarity will only work until it is counterbalanced by pressure forces of air that remains inside the MOF. In these situations, more complex setups may include micropumps, syringes [12] or lateral openings that enhance fluid diffusion times [17].

2.3 Spectroscopy, Functionalization and Non-Linear Effects

One of the available techniques for fluid sensing with MOFs consists on exciting a liquid or gas either with a broadband source or a tunable laser and measuring its *absorption spectrum* in reflection or transmission. Molecules generally show several characteristic vibrational absorption lines in the visible and near-IR region that can be excited and monitored using available optical fiber equipment [15, 18]. Spectroscopical analysis of analytes avoids the need for sensor functionalization, reducing the sensor's manufacturing complexity and increasing its stability over time since there is no functionalized surface degradation [5, 12]. This technique has been used to detect industrially relevant gases

[2]The equivalent free-space interaction length gives the length that a MOF should have such that the cumulative interaction of light with a fluid is the same as a unit length of free-space light propagation through the same fluid. It is a useful concept to compare MOFs in terms of their interaction efficiency and it is strongly influenced by the hole power fraction. As an example, a MOF with a hole power fraction of 50% has an equivalent free-space length of 2 m.

such as acetylene, methane, hydrogen and volatile organic compounds.

Even so, *functionalization* allows the detection molecules that do not have such characteristic spectral features. Usually a fluorescent label with well defined spectral properties is used such as quantum dots or organic dyes [18]. Quantum dots are particularly promising in this matter due to their photostability and flexibility in terms of multiplexing and functionalization which enable applications with great specificity [19]. MOF fluorescence spectroscopy has been used to detect complex molecules such as caffein, antibodies and DNA strands.

Non-linear effects such as *Raman Scattering*, *Four Wave Mixing* and *Surface Plasmon Resonance* (SPR) can also be exploited for fluid sensing [12]. In particular, SPR appears as an increasingly interesting solution in biochemical sensing. SPRs are guided modes that exist at a metal–dielectric interface. By coating the holes of an MOF with a metal like gold, SPR modes are allowed to propagate inside the optical fiber. When the holes are filled with a certain fluid, the effective refractive index of the SPR mode is altered, resulting in measurable spectral changes. One can then identify a solution by measuring its refractive index. SPR-based sensors are one of today's hot topics in MOF sensing and high resolutions have been achieved with this type of sensors. Fig. 2.2 shows the results of simulations performed by Bing et al. [20] in which a metal layer was deposited on the larger holes of an MOF, represented in Fig. 2.2 (a). Both core and SPR modes are displayed in Fig. 2.2 (b) as a function of transverse position across a specific fiber axis (white dashed line in Fig. 2.2 (a)).

2.4 Interferometric Configurations

Interferometry is recurrently used in optical sensing since it enables the creation of sensors with high dynamic range, accuracy and sensitivity [13]. The basic principle is the *interference* of light waves that follow different optical paths. By changing physical or chemical environmental parameters such as temperature or fluid concentration, one or more optical paths are changed, which translates to information that can be retrieved by measuring phase, wavelength, visibility or others.

Essentially, interferometers vary on their beam splitting and recombining mechanisms and can be characterized accordingly. Noteworthy are Fabry-Perot, Mach-Zehnder,

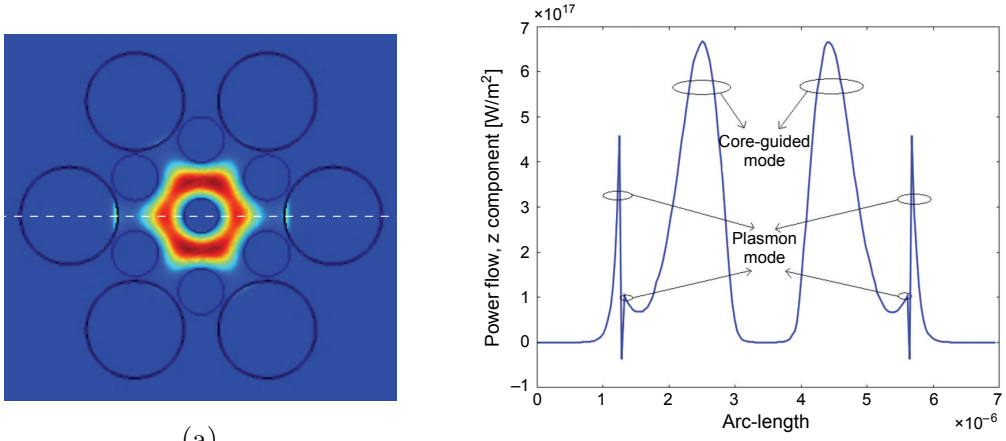

(a) (b)

Figure 2.2: **(a)** Simulation of power flow in an MOF where the larger holes are coated with a metal layer. The power profile is plotted in **(b)** as a function of position across the dashed white line, where both guided and SPR modes are visible. Figures reproduced from [20].

Michelson, Fiber Loop Mirror and modal interferometers.

Fabry-Perot interferometers consist on two surfaces that divide the incoming beam in reflected and transmitted components. Fig. 2.3 (a) has two examples of fiber Fabry-Perot interferometers where the surfaces are either the interfaces between the fiber and air (top figure), or, in general, two surfaces with reflection coefficients R_1 and R_2 (bottom figure). These surfaces form a cavity that can be fabricated using etching, FBGs, metal films or simply by splicing an MOF to an SMF.

The spectrum of a classical Fabry-Perot interferometer has several peaks with finesse and visibility that depend on the reflectivity of the cavity surfaces and a free spectral

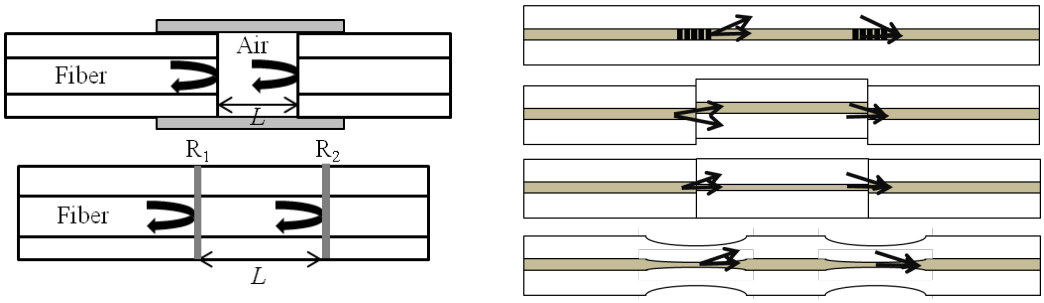

(a) (b)

Figure 2.3: Examples of **(a)** Fabry-Perot and **(b)** Mach-Zehnder fiber interferometers. Figures reproduced from [13].

range (FSR), distance between consecutive peaks, given by

$$\mathrm{FSR} \approx \frac{\lambda^2}{2nL} \tag{2.1}$$

where λ is the wavelength of one of the peaks considered, n is the refractive index of the cavity and L is the cavity's length [21]. More generally, $2nL$ is the optical path followed by light that enters the cavity. From equation 2.1 it is clear that changes either in refractive index or cavity length will translate in measurable spectral features. Indeed this is the principle of Fabry-Perot sensors that measure strain (which directly changes L), temperature (which can either change L by thermal expansion or n through thermo-optical effects) or fluids (which have different refractive indexes).

Fabry-Perot interferometers are very easy to create. In fact, if one excites an optical fiber during the splicing alignment process and analyzes its reflection, it is possible to observe the characteristic Fabry-Perot spectrum changing as the distance between fibers changes. Fig. 2.4 (a) shows this effect for various distances between fibers, manually controlled with an electric-arc fusion splicer, and (b) is a plot of the FSR as a function of cavity length where the $1/L$ dependency can be clearly observed.

In *Mach-Zehnder* and *Michelson interferometers*, light is divided in two arms, in which one of the arms interacts with the measurand and the other is kept isolated to serve as a reference [13, 22, 23]. When light is recombined, the interference pattern between both arms will vary with the phase differences that the sensing arm suffers. The usual procedure

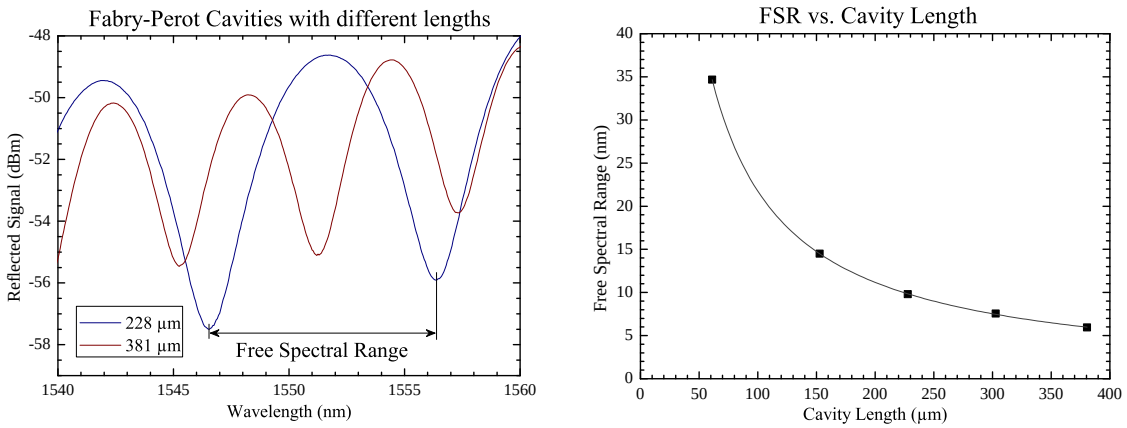

(a) (b)

Figure 2.4: **(a)** Spectrum of Fabry-Perot cavities with different cavity lengths and **(b)** plot of the free spectral range as a function of cavity length.

consists on using the fiber core as the reference arm and cladding modes as the sensing arms, since these are closer to the external environment. Several methods can be used to divide light and couple it to cladding modes. Fig. 2.3 (b) shows some examples, such as (from figure top to bottom) Long Period Gratings, fibers spliced with a transverse offset, fiber segments with smaller core diameters and tapers. Mach-Zehnder interferometers can also be built with MOFs by collapsing the fiber structure which broadens the input beam from an SMF and allows excitation of cladding and core modes [24]. Michelson interferometers distinguish themselves from Mach-Zehnder ones from the fact that beams are reflected back and are recombined by the same element that performs beam splitting. The fact that each beam goes through the same optical path twice can be harnessed to obtain sensors with higher sensitivity.

Fiber Loop Mirrors use interference effects between counter-propagating beams in an optical fiber loop [13, 22]. This type of interferometer has seen great application in gyroscopes [4]. When a fiber loop rotates around the axis perpendicular to the loop, a phase difference between both beams is created due to the different flight times induced by the rotation. Fiber Optic Gyroscopes where first developed in 1981 by Bergh et al. [25] and today are used on critical industries such as aerospacial or military. Fiber Loop Mirrors can also employ interference due to polarization effects (fig. 2.5 (a)). In this matter, Highly-Birefringent (HiBi) MOFs are used due to their strong polarization-dependent response. For example, in an MOF with two small holes positioned symmetrically in relation to the fiber's core, one of the polarizations will observe stronger variations in effective refractive index if the holes are filled with a fluid than the other polarization, resulting in a measurable interference pattern change.

Modal interferometry is the general case of the above mentioned configurations, where the relative phase difference between two or more modes inside a fiber is exploited [26]. Modal interferometers have become commonly implemented in MOF-based sensing configurations due to their simplicity. In many cases, MOFs support more than a single propagation mode. When excited by an SMF, several modes will propagate through the MOF. These can be recombined and interefometric measurements can be performed [27].

Fig. 2.5 (b) has an example of a modal interferometer where light from an SMF is broadened by the collapsed structure of a PCF and excites two core modes [26]. Since the PCF modes have different hole power fractions, their effective refractive indexes differ.

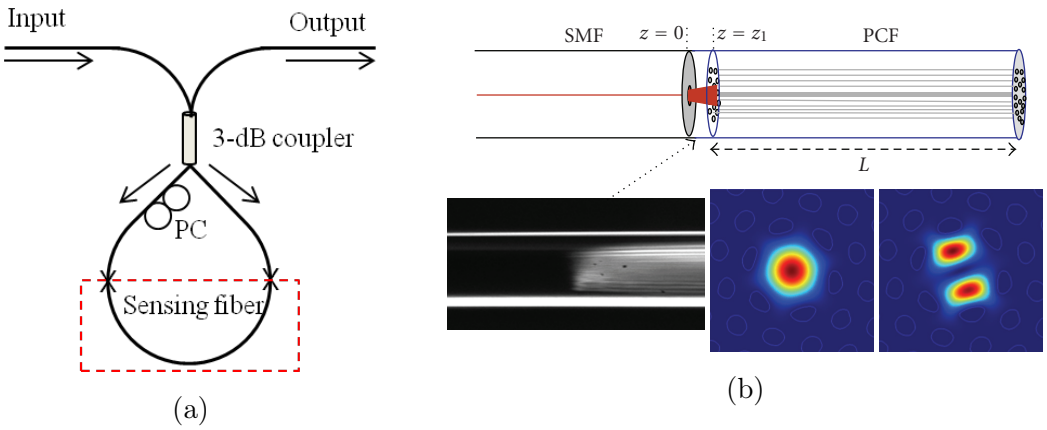

Figure 2.5: (a) General scheme of a Fiber Loop Mirror interferometer. Figure reproduced from [13]. **(b)** Example of a Michelson modal interferometer where light from an SMF is broadened by the collapsed structure of a PCF subsequently exciting two core modes Figure reproduced from [26].

Light is reflected at the cleaved end of the MOF and interference is analysed in a reflection setup. The open holes of the PCF can be exploited for fluid sensing since the RI of each mode depend differently on the RI inside the fiber's holes.

It should be noticed that due to the existence of several cladding propagation modes, Mach-Zehnder and Michelson interferometers may usually include additional modal interference effects since when coupling light with the cladding one does not necessarily excite a single cladding mode.

2.5 Conclusion

Since the development of optical fiber fabrication techniques, sensing applications have been continuously researched. These efforts have become more intense with the growth of optical telecommunications which lowered the costs of standard optical fiber equipment. MOF-based sensors usually rely on this generally available equipment in order to try to keep fabrication costs as low as possible, reducing the effort of bringing proof-of-concepts to the actual market.

That being said, the pursuit for new fiber sensors is usually performed by developing new MOF designs and studying their application in the configurations described in this chapter. This is a very promising field taking into consideration the versatility of microstructured fiber designs for particular applications. Several techniques such as spectroscopy or non-linear effects can be used either for specific or non-specific sensing.

Specificity can be increased by surface functionalization, although this step increases the cost and complexity of sensing schemes. Much work has been done on non-specific refractive index sensing by harnessing the potential of interferometric setups. In these, small refractive index changes translate into phase differences between propagation modes which can result in very high sensitivities and resolutions.

Nowadays, MOF sensors have been created for a large variety of chemical and biochemical analytes. Note should be given to the regular reviews of Wolfbeis on chemical and biological fiber sensing which have been covering the field in depth since 1997 [10]. Although these reviews do not focus on MOFs, they are organized by analyte and allow the reader to quickly check the state-of-the-art for the specific fluid that he/she intends to study.

Based on this overview, chapter 3 will present the fabrication procedure of a 5-hole caterpillar-inspired MOF which could in the future be used for fluid sensing applications, and chapter 4 will report a novel approach to the study of volatile organic compounds using the holes of an MOF to track the evaporation dynamics of these types of fluids.

Chapter 3

Fabrication and Post-Processing of a Caterpillar-Like Fiber

3.1 Introduction

The present chapter contains a detailed contextualization of Microstructured Optical Fibers (MOFs) through an overview of their origin and also through the presentation of their splicing and fabrication techniques. The fabrication of an MOF whose cross-section contains five holes placed in the same axis, apparently resembling a caterpillar, is described. After fabrication, the caterpillar MOF was put through a post-processing step in order to create microfluidic channels for future applications in fluid sensing. For this, a Focused Ion Beam, whose main working principles are overviewed here, was used to alter the structure of the MOF at a localized micrometric scale.

3.2 Overview of Microstructured Optical Fibers

The earliest account of an MOF was documented in 1974 [28]. In this work, a single-mode fiber composed only of a pure fused silica core surrounded by large air holes was reported (fig. 3.1 (a)), eliminating the need for doping either the core or cladding.

Afterwards, it was thought that one could design fibers with new guiding properties by tailoring the cross-section at a subwavelength level, extending the ideas of 2-dimensional photonic crystals to full 3D structures [29]. In 1996 the concept of a *Photonic Crystal Fiber* (PCF) was realized by building a hexagonal structure composed of air-holes with

a silica core in its center (Fig. 3.1 (b)) [30]. By adjusting the ratio between the core's diameter and the distance between air holes (pitch), this type of fiber could operate in single-mode for any desired wavelength within the inherent limits of silica [31]. This fiber is classified as an index-guiding *Total Internal Reflection* (TIR) PCF since light is guided through total internal reflection, similarly to conventional step-index fibers.

Soon afterwards, in 1999, the same group of researchers presented the first hollow-core *Photonic Bandgap Fiber* [32]. In these fibers the cladding is designed in a way that blocks the propagation of certain wavelength intervals. Thus, one can have light propagating within a hollow core unable to escape to the cladding due to these photonic bandgaps (Fig. 3.1 (c)).

The area of MOFs has since grown to form an important research community. Figure 3.2 contains several examples of the wide variety of geometries that can be fabricated for different applications. Although most MOFs discussed in this document are composed only of fused silica and air holes, it is possible to create fibers with a variety of materials, for example rare earth doped silica or calcogenide glass. Several review papers have been published on the topic of MOFs [14, 29, 36–38], detailing the prolific advancement of its existing and potential applications. Some interesting examples include supercontinuum and laser light generation, high resolution spectroscopy, broadband zero chromatic dispersion propagation, high power transmission, particle trapping and guiding (optical tweezing), enhanced nonlinear interaction with fluids, and gas and liquid sensing.

3.3 Splicing and Fabrication Techniques

Although promising, the complex structure of microstructured fibers can hinder their integration in conventional optical fiber systems, namely in terms of the fabrication procedure, MOF-SMF splicing and propagation losses.

Whilst the fabrication of MOFs can seem intricate due to their elaborate cross-section designs, the process is in fact similar to that of SMF production [12, 36, 39]. Despite being able to produce MOFs by *extrusion* of molten glass through a die with the desired cross-section (fig. 3.3 (a)), this technique applies mainly to soft glasses [29]. As such, MOFs are in general fabricated by building a preform, either through *capillary stacking* or glass *drilling*, and by drawing the preform just like in conventional SMF fabrication.

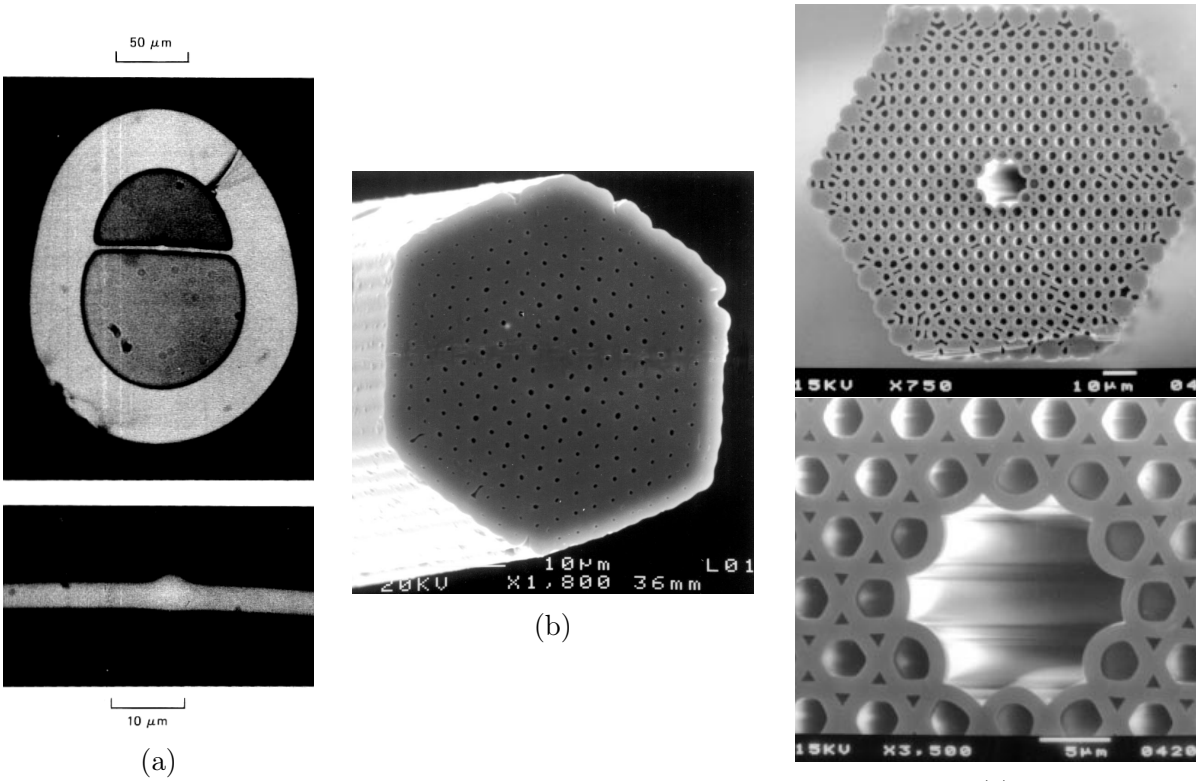

(a) (b) (c)

Figure 3.1: **(a)** Image of the earliest report of a single-mode, single-material MOF with detailed view of the core region. The core is supported by a silica slab surrounded by two large air holes. Figure reproduced from [28]. **(b)** A SEM image of the first index-guiding PCF where the small silica core is observable at the center of a periodic hexagonal air-hole structure. Figure reproduced from [30]. **(c)** A SEM image of the first hollow-core PCF with a zoomed view of the core region. Figure reproduced from [32].

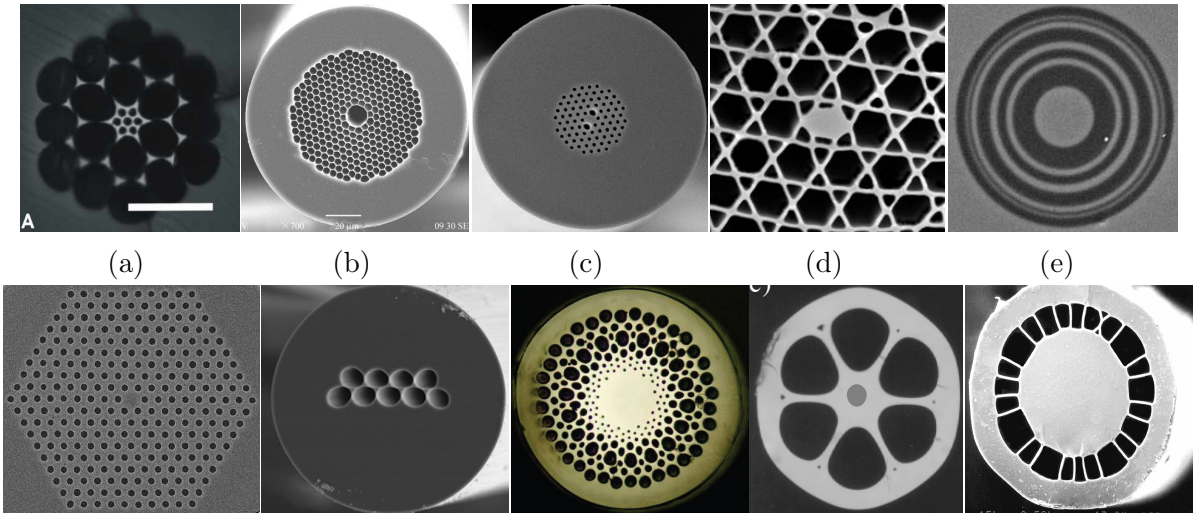

(a) (b) (c) (d) (e)

(f) (g) (h) (i) (j)

Figure 3.2: Examples of the wide variety of existing MOFs. Figures reproduced from: **(a)** [15]; **(b)** and **(c)** [14]; **(d)** [16]; **(e)** and **(f)** [29]; **(g)** [33]; **(h)** [34]; **(i)** and **(j)** [35].

In *stack-and-draw* procedures, the preform is built by stacking several glass capillaries in order to obtain the desired fiber design in a relatively large diameter of $\sim 20\,\text{mm}$. This allows an almost arbitrary definition of fiber properties such as pitch (distance between neighbouring holes), core diameter and hole spatial distribution that will affect the final refractive index profile. The preform is brought to a fiber drawing tower and it is either drawn directly to the desired fiber diameter, or an intermediate preform is created by drawing the original one down to millimeter scale. This intermediate preform may once again be drawn in order to achieve MOFs with smaller features, down to μm scale – *multiple thinning*. During the whole process, environmental parameters like pressure or temperature are controlled in order to further modify the fiber's final structure. For example, the capillaries can be dilated by increasing their inner pressure during the drawing process and in this way obtain a fiber with larger holes. Fig. 3.3 (b) represents a simplified stack-and-draw fiber fabrication process.

After fabrication, the practical use of MOFs is limited by the ability to merge them with

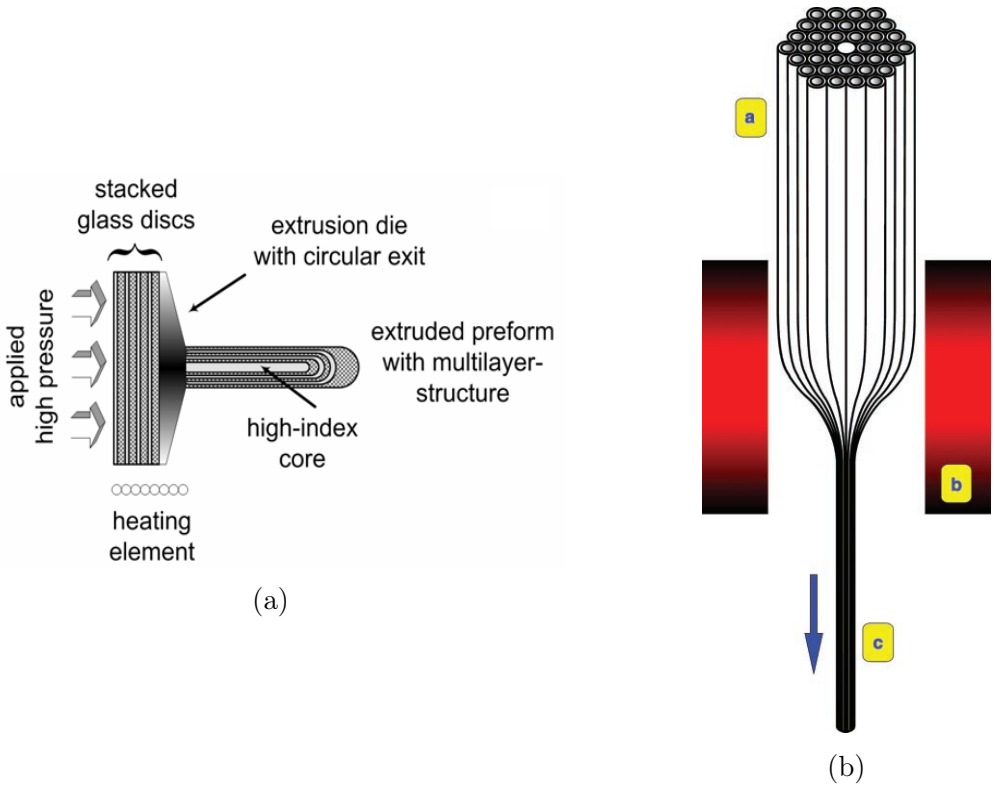

Figure 3.3: **(a)** Extrusion of a Bragg fiber from a multilayer of stacked glass discs. Figure reproduced from [40]. **(b)** In the stack-and-draw technique, glass capilaries are a) stacked together, b) fused in a furnace at $\sim 2000\,^{\circ}\text{C}$ and c) drawn into fibers. Figure reproduced from [37].

conventional optical fiber technology. Ideally this should be achieved by the ubiquitous electric-arc fusion splicing technique.

Although better control of the splicing process can be achieved with resistive heating elements [38], several authors have reported results and optimization procedures on fusion splicing MOFs with an SMF using electric-arc discharge [14, 41]. The main idea is that since MOFs have a smaller volume of silica, the amount of energy that needs to be delivered so that glass is fused is smaller than in the case of an SMF. As such, authors start with the standard fusion parameters of SMFs and optimize them in order to lower splicing losses or reduce the effect of the electric-arc on the MOF structure. Usually the affected parameters are discharge current, discharge duration and offset between the center of the electric-arc and the interface between both fibers (fig. 3.4 (a)).

Often, mode field mismatch between both fibers can be one of the main loss mechanisms in splices [14, 38]. Mode field compatibility can be attained by creating slowly varying core taper regions that match MOF and SMF mode profiles (fig. 3.4 (b)). Oppositely, hole collapse can affect applications where the structural integrity of the MOF is critical. This can be minimized by calibrating the fusion parameters so that the MOF is far from the center of the discharge area and the current is as small as possible while guaranteeing good adhesion between both fibers [41].

Notwithstanding, there is no definite procedure on how to correctly splice a MOF and ultimately this process has to be optimized for the specific MOF in use and the application which one envisages.

The ability to produce and connect highly versatile microstructured fibers with conventional ones does not however solve all the drawbacks of MOFs. Despite having the

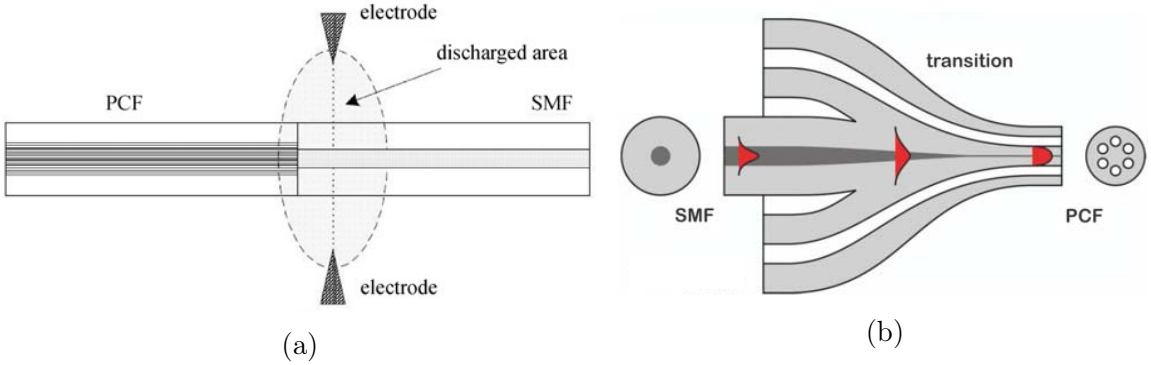

Figure 3.4: (a) Electric-arc offset for splice loss reduction. Figure reproduced from [14]. **(b)** A slowly varying taper for mode field matching. Figure reproduced from [38].

possibility of specifically designing a MOF to obtain low propagation loss, in general these have values $2-3$ orders of magnitude higher than that of SMFs ($\sim 1-10\,\mathrm{dB\,km^{-1}}$) [14]. This is mainly due to the difficulty in maintaining homogenous conditions during the fiber drawing process, which leads to loss-inducing structural defects. Intrinsic loss remains the main limitation of MOFs in conventional SMF telecommunication circuits and restricts the maximum fiber length that one can use. Even so, in applications where loss is not such a critical aspect or where shorter lengths of fiber are needed, microstructured fibers have created new lines of innovative engineering approaches.

3.4 Fabrication of a caterpillar-like MOF

In this dissertation, a new MOF design is presented, motivated by the need for novel fiber optic devices to perform studies on the interaction of light with fluids. The proposed fiber (fig. 3.5 (a)) consists on a five-hole MOF, with a structure resembling that of a caterpillar (fig. 3.5 (c)). In order for this MOF to be spliced with SMFs, the diameter should be around $125\,\mu$m to guarantee optimum splice integrity and resistance. Since the holes will be filled with fluids, previous experiences have shown that these should have a minimum diameter of $10\,\mu$m to allow fluid flow across the holes. Finally, in order to build fiber interferometers, the cavities should be close enough to allow evanescent field coupling of neighbouring holes. The hole spacing should thus be as short as possible, with a maximum value of $\sim 1\,\mu$m.

Taking into consideration the desired parameters, a glass preform structure that could be drawn into the proposed 5-hole MOF was designed. The preform is shown in fig. 3.5 (b). It has 91 glass elements stacked in a hexagonal structure. First, 91 pure fused silica glass rods were manually cleaned and stacked. Afterwards, five rods in the center were substituted by hollow capillaries with a wall thickness of $100\,\mu$m. Each element has a diameter of 1 mm and a length of 50 cm, which makes the preform 11 mm wide and 50 cm long. Finally, the stacked preform was inserted in a glass jacket for additional structural integrity, increasing the final width to ~ 13 mm. A glassblower then fixed all these elements by fusing the end tips.

In order to manufacture the desired MOF, the intersticial air in the hexagonal structure and between this one and the circular glass jacket must be removed during the

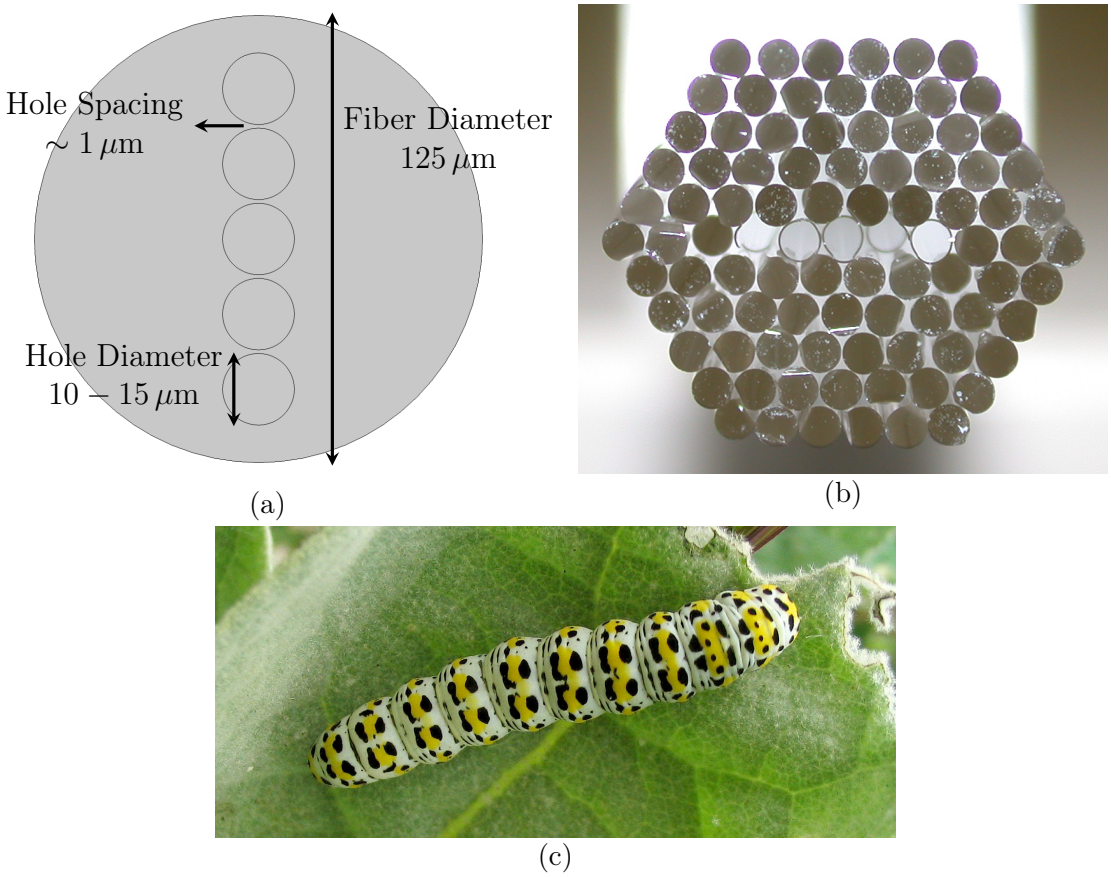

Figure 3.5: **(a)** Cross-section parameters and **(b)** preform of the fabricated microstructured fiber inspired on a **(c)** caterpillar. Picture reproduced from [42].

drawing process, whereas the capillaries' structure should be maintained. To accomplish this, pressure outside the capillaries needs to be reduced to very low values to obtain a homogenous glass cladding and a positive pressure difference between the capillaries and the intersticial volume should be created to guarantee that the former do not collapse. For this purpose, intersticial pressure was actively reduced with a rotary mechanical vacuum pump, whereas the capillaries were closed by fusing both ends. Consequently, in order to control the fiber structure during drawing, pressure inside the capillaries must be controlled passively, eg. by changing the drawing tower's oven temperature, or the intersticial vacuum pressure.

Following the stacking process, the preform was brought to the drawing tower. Three different fiber structures were drawn, each with a length of 100 m, the difference among them being the drawing temperature which alters the pressure diference and, consequently, the fiber's cross-section. The fiber turned out to be very fragile and the drawing conditions

were changed whenever the fiber broke during the drawing process. Optical microscopy pictures of the three samples is shown in fig. 3.6. Each sample is associated with a codename, which is indicated under the corresponding picture. The effects of varying pressure can be seen on the structure of the five central hollow-cores. While the holes of the first sample (a) seem to be the ones which most resemble the circular holes that we designed, sample 661b3 (c) seems to have the most homogeneous structure of the three. Rough measurements indicated that sample 3 has a hole width of $\sim 10\,\mu$m and height $\sim 20\,\mu$m, with submicrometric inner wall thickness. Since these values are in agreement with the initial design, the drawing process was stopped and the remaining preform was kept for future experiments. Only approximately 10 cm of preform was used in this process. Also, afterwards no efforts towards precise structure optical measurements were made, since it was already planed that we would be using a Scanning Electron Microscope, integrated in a Focused Ion Beam for fiber post-processing, which allows for greater resolution microscopy.

All samples proved difficult to handle, with very fragile structures. Even so, it was possible to find near-optimal parameters for fusion-splicing the fiber to an SMF without structural collapse near the electric-arc discharge region. Splicing was performed using a Sumitomo Electric T-36. An offset of approximately one quarter of the machine's horizontal screen range was manually applied, away from the arc discharge center, in the direction of the MOF. The splicing parameters are indicated in table 3.1.

Preliminary tests were performed on filling the holes with fluids. A few-milimeter MOF

(a) 661b1 (b) 661b2 (c) 661b3

Figure 3.6: Cross section of the end tip of the three fiber samples that were drawn. Images obtained by optical microscopy.

Table 3.1: Near-optimal parameters for splicing the caterpillar MOF using a Sumitomo Electric T-36 with an offset away from the arc discharge.

Parameter	Value
Arc Duration	0.55
Arc Gap	10.00
Arc Power	10
Prefusion	0.10
Overlap	15.00

segment was fusion spliced to a SMF. The open end of the MOF was dipped in several fluids and the filling process was analysed with an optical microscope. Volatile organic compounds such as acetone or isopropanol fill the holes and evaporate easily, although with frequent formation of air bubbles. When the fiber was immersed in a Refractive Index Fluid with $n_D^{25\,^\circ\mathrm{C}} = 1.46$, the formation of air bubbles proved to be a critical factor that hindered the homogenous filling of the MOF.

Additionally, to build an in-line sensing setup, the manufactured MOF has to be fusion spliced to SMFs on both ends as in fig. 3.7 (a). This makes it impossible to modify the contents of the fiber's interior after the fabrication of the device.

Both problems should in principle be solved by creating microfluidic channels close to the spliced region that allow bubbles to escape and liquids to be inserted. Several possibilities for this arise. The simplest approach would be to create channels near one of the splices (fig. 3.7 (b)), although, as mentioned previously, the formation of air bubbles impedes the complete filling of the MOF. As such, microfluidic channels must be drilled in a way that enables flow on both ends of each hole such as in fig. 3.7 (c). One way to pursue this solution is to create the microchannels using a Focused Ion Beam. The following section provides an introduction to Focused Ion Beam technology before proceeding to the description of the caterpillar fiber post-processing.

3.5 Focused Ion Beam

Focused Ion Beam (FIB) is a technique used in nanotechnology for material micro and nanomachining. Its importance grew due to its applications in the semiconductor industry and TEM sample preparation since it is a very versatile technique that allows

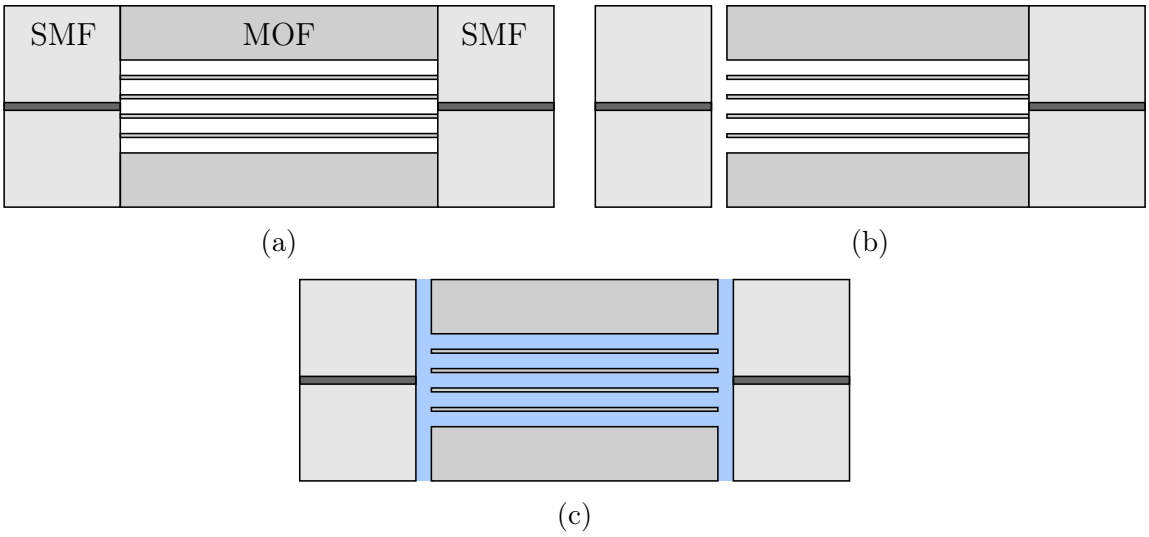

Figure 3.7: Possible longitudinal profiles of an in-line MOF sensing element, fusion spliced to SMFs: **(a)** fluid flow inside the holes is not possible if both ends are sealed; **(b)** if microchannels are opened to the outside only on one end, air bubbles will form inside the holes; **(c)** if microchannels are opened on both ends of the MOF, homogenous hole filling becomes possible.

substrate sputtering, imaging and implantation down to nanometric resolution [43, 44].

The principle of operation is to accelerate ions from a source (typically a Ga liquid-metal ion source) and focus them on a sample. Ion acceleration and focusing is performed in an *ion column*, whereas the sample is located in a separate high vacuum chamber. Incident ions remove material from the sample, a process which releases neutral atoms, ions and electrons. If the ion current is high enough, the FIB can effectively be used for substrate *milling*. Milling is performed through sputtering, resulting from the collision of ions with the sample when the incident energy is higher than the sample's surface binding energy. However, if energy is too high, ion *implantation* becomes a relevant effect, which can either be a source of unwanted sample amorphization and doping, or a way to usefully modify sample properties, for example to subsequently etch the implanted region.

Another relevant effect during milling is the *redeposition* of sputtered material. This effect becomes increasingly important when the depth of the structure that is being created increases since the solid angle through which sputtered matter can escape decreases with increasing depth. Redeposition can be countered by sample post-processing, where additional milling steps are taken to remove redeposited material, or by choosing a more appropriate milling mode. Milling is performed by scanning the beam on the sample ac-

cording to the wanted structure design. Two milling modes can be used: *plane-by-plane mode*, in which the ion beam scans the sample several times, each time removing a plane with a small depth until the final depth is obtained; and *polishing mode*, in which the structure is created directly with the wanted depth on a single beam pass. While in general plane-by-plane is preferred over polishing since redeposited material is consecutively removed on each plane scan, in some situations polishing can achieve better results, as it will be seen in the following section.

Ions and electrons removed from the sample can be used for *imaging* the substrate. However, since FIB imaging is inherently destructive, often machines also include Scanning Electron Microscopy (SEM) equipment that can be used to monitor the milling process while avoiding the unnecessary removal of additional material from the sample. Fig. 3.8 shows a side view of the geometry of a TESCAN LYRA FIB-FESEM Focused Ion Beam, where separate FIB and SEM columns can be seen, with an angle of 55 ° between them.

Recently there has been interest in bringing the flexible capabilities of the FIB to optical fiber sensing. A FIB allows for high resolution tailoring of an optical fiber and a variety of structures can be built, such as cantilevers for atomic force microscopy [46] or gratings for sensing [47].

By post-processing microstructured fibers with focused ion beam it is possible to create endless device variations. As an interesting example, a sensing head composed of a MOF

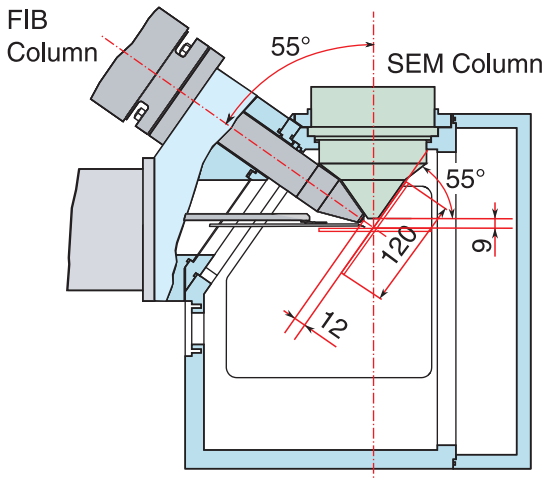

Figure 3.8: Side view of a TESCAN LYRA FIB-FESEM Focused Ion Beam. Figure reproduced from [45].

with a P_2O_5-doped cladding was etched with a HF solution, creating a 15 μm nanowire. The authors then used a FIB to create a thin gap in the nanowire, resulting in a cylindrical cantilever structure that was able to measure vibration [48].

Another group of researchers has reported the fabrication of side channels in microstructured fibers to allow fluid flow using a FIB instead of laser ablation or femtosecond machining, while avoiding additional etching steps and maintaining high resolution processing [49]. Thus, this technique has proved to be a successful way to create microfluidic channels in MOFs, such as required in the case of the fabricated 5-hole MOF. In the following section, the post-processing of this fiber is presented.

3.6 FIB Processing

In order to create microfluidic channels on the caterpillar MOF, a TESCAN LYRA FIB-FESEM Focused Ion Beam was used. Fig. 3.9 schematically represents the procedure: the FIB is focused on the tip of a 5-hole MOF and it is configured to remove glass from the regions marked by the red dashed lines. By milling these regions down to a certain depth, the microchannels are created.

FIB samples have to be electrically conductive in order to be able to visualize them with the integrated SEM. As such, a 50 nm Ta layer was deposited by sputtering in all fiber samples. Afterwards, short conductive MOF segments were fixed in a metallic sample holder using either aluminum adhesive or silver spray. Each sample holder was able to carry 4 different fibers. However, due to electric charging effects, not all samples were usable at the FIB since these effects cause strong vibrations that obstruct any SEM or FIB experiments. This problem may arise from non-homogeneous metal deposition during the sputtering process or weak adhesion of the gluing elements. On this matter, silver spray resulted in better results than aluminum adhesive.

Using the TESCAN machine, it was possible to obtain more precise measurements of the MOF using the integrated SEM. Pictures of the three samples' cross sections are seen in fig. 3.10. In particular, for sample 661b3 (fig. 3.10 (c)), the hexagonal profile has an average diameter of 120 μm. The holes have an average width of 11 μm and height of 22 μm. Although not perfectly round as initially designed, the hole dimensions accomplish our minimum requirement of 10 μm in both directions perpendicular to the fiber's length

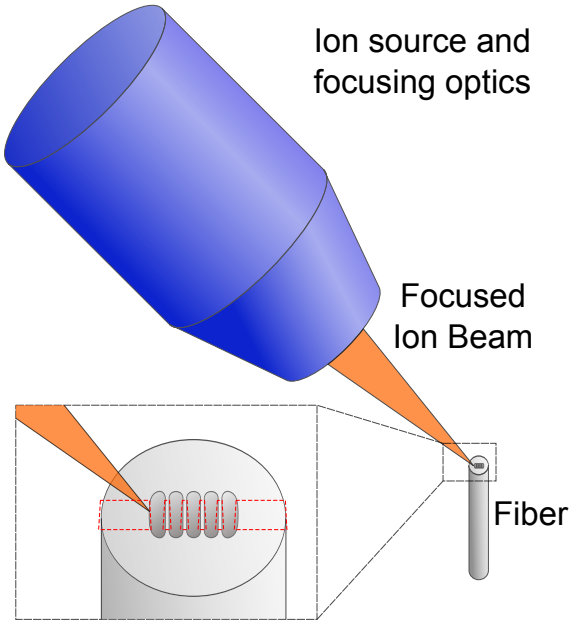

Figure 3.9: Cross section of the three MOF samples and close up of 661b3's holes. Images obtained by Scanning Electron Microscopy.

(fig. 3.10 (d)). The most surprising feature of this fiber is the small 0.3 μm wall thickness which should guarantee a large coupling between all five holes, as requested.

Fiber 661b1 was not used since it proved to have the most fragile structure of the three during simple fiber handling processes such as cleaving and splicing. Also, its structure varies strongly along its length, probably since it was the first fiber to be drawn and in the beginning of the drawing process some time is needed for the system to reach stable drawing conditions. Similarly, fiber 661b2 was discarded since most of its samples had their internal walls broken. This problem may have arisen during the drawing process. When the fiber broke, the shock wave may have propagated through this sample and destroyed the inner wall structure, a frequent problem in fibers with sub-μm features. As such, most work was performed on samples from fiber 661b3.

Initially, in order to test the FIB's capabilities on this MOF and to gain technical sensitivity on how to best handle the machine in this particular application, some fiber samples were processed using a variety of approaches. In particular, trials were carried to find out which settings worked best in terms of ion beam intensity, milling operation mode (plane-by-plane or polishing) or angle between fiber and FIB. Fig. 3.11 (a) shows

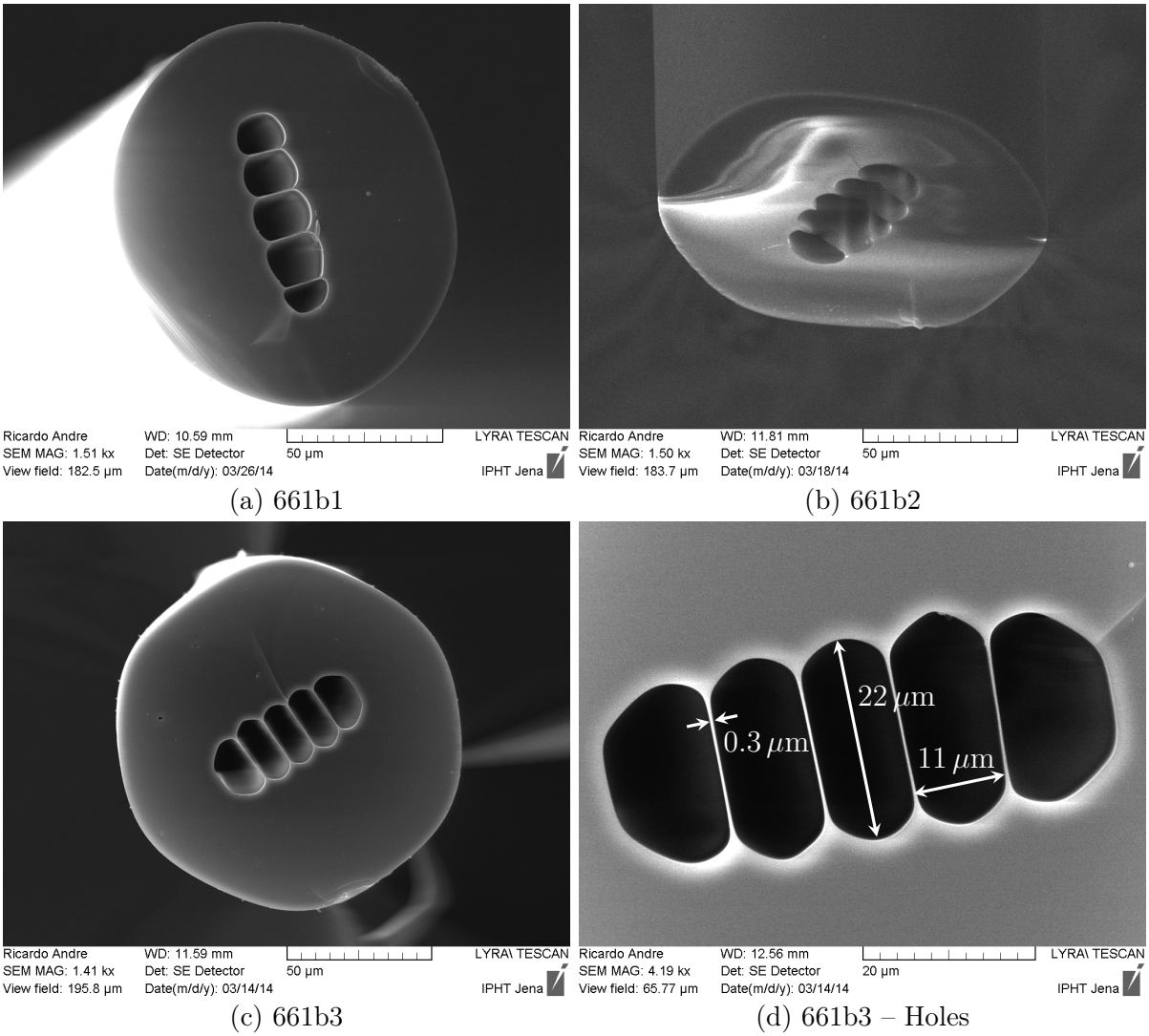

(a) 661b1 (b) 661b2

(c) 661b3 (d) 661b3 – Holes

Figure 3.10: Cross section of the three MOF samples and close up of 661b3's holes. Images obtained by Scanning Electron Microscopy.

the first processed 5-hole MOF. Detailed views of the microchannels can be found in figs. 3.11 (b) and (c). Both channels were created using plane-by-plane milling, with a ion beam current of 7.3 nA and with parallel alignment between fiber and FIB, ie. with the FIB column and the fiber's axes aligned. The machine was programmed to create a 10 μm-deep channel on the left side and 20 μm on the right, both 10 μm-wide. Each milling process took 15 min and 30 min respectively, even though the current was close to its maximum. It was observed that this milling mode results in a final depth which is less than half of the programmed one, and creates much deeper channels on both ends, as visible in figs. 3.11 (b) and (c), which may be due to the higher solid angle through which the extracted matter can escape the fiber, avoiding redeposition effects.

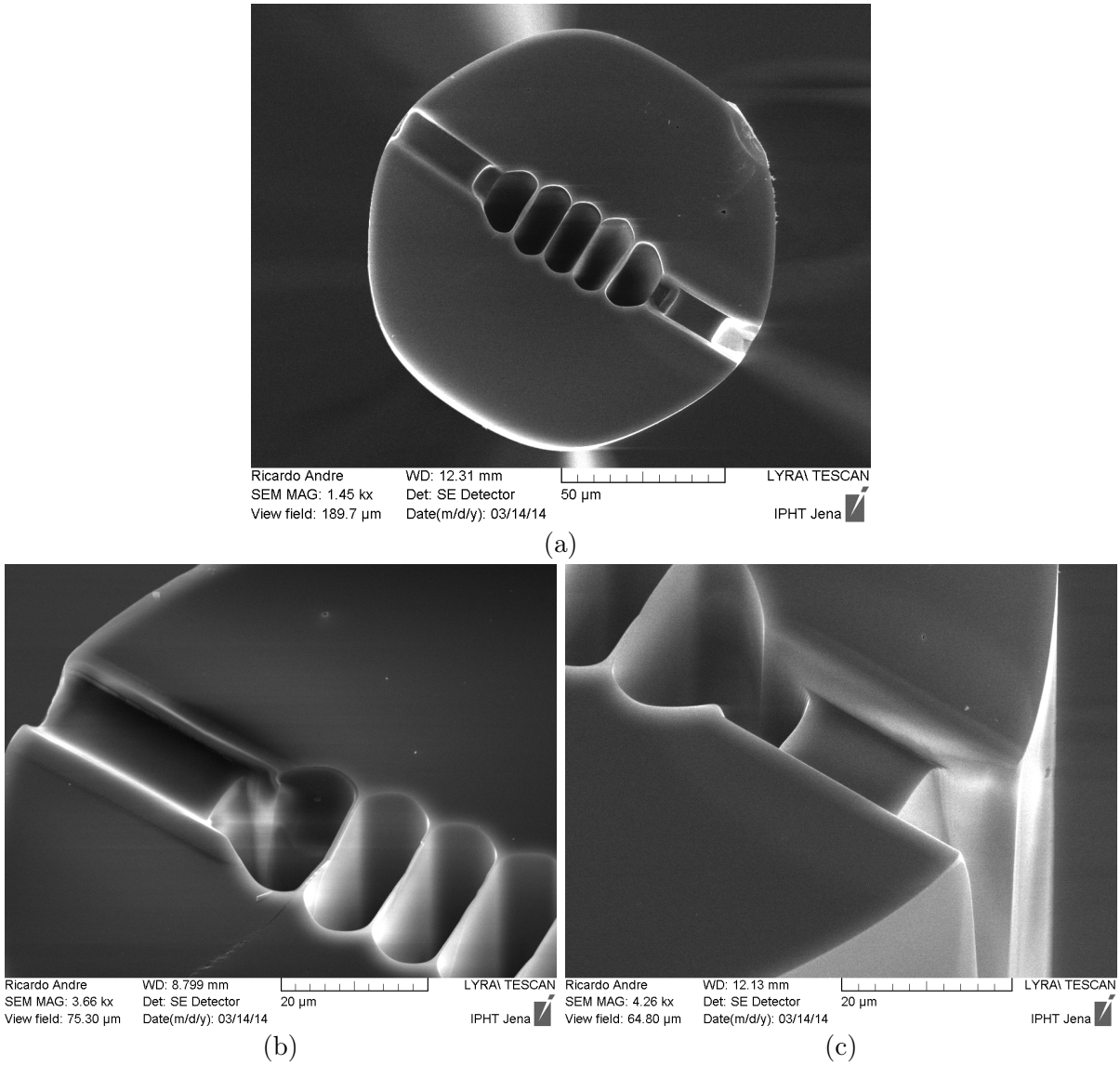

Figure 3.11: SEM images of the first processed 5-hole MOF: **(a)** shows two large microchannels to the external environment; **(b)** is a detailed view of the microchannel on the left side; and **(c)** is a detailed view of the microchannel on the right side.

A second trial, now using polishing mode, can be observed in fig. 3.12 (a). In this fiber, the channel on the left was polished from inside out, while the channel on the right was polished inversely, from outside in. It is possible to notice that the leftmost inner wall is much thicker than the others due to redeposition of the polished silica. It can also be noticed that polishing is quicker than plane-by-plane milling: while for the previous sample it took half an hour to drill a channel approximately 8 μm-deep, on the second sample it took 45 min for a $\sim 15\,\mu$m-deep channel. As such, for microchannel milling with parallel fiber-FIB alignment, the best approach would be to polish from outside in. Fig.

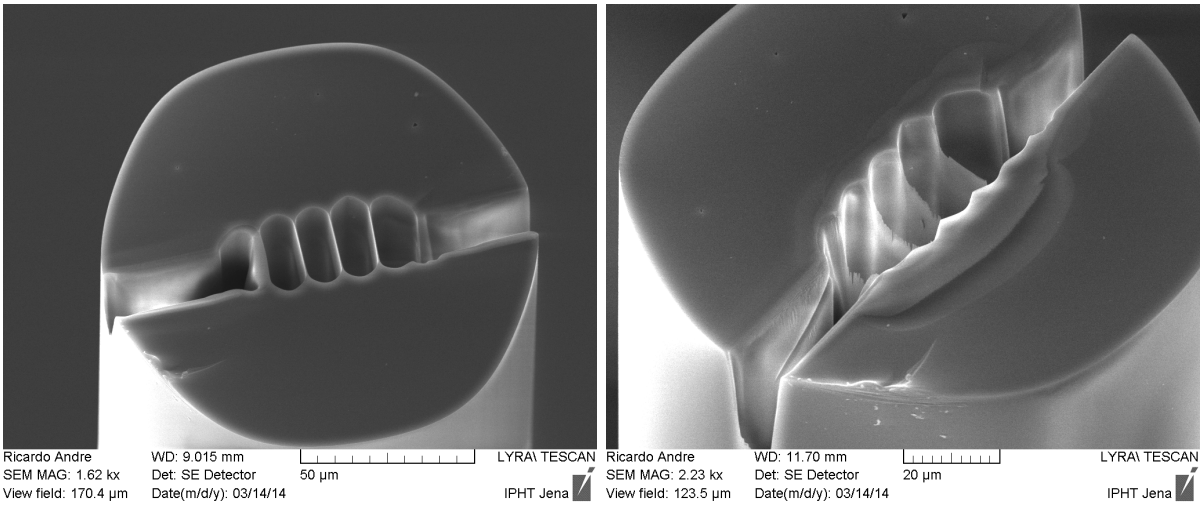

(a) (b)

Figure 3.12: SEM images of the second processed MOF before **(a)** and after **(b)** removing the inner walls.

3.12 (b) shows the result of a preliminary plane-by-plane milling trial of the inner walls. By carefully analysing the final result, one can observe that this procedure leads to further inner wall thinning, which may be a source of increased sensor frailty and eventually result in wall collapse, as in sample 661b2.

An alternative to colinear fiber-FIB alignment would be to position the fiber axis perpendicular to the ion beam. Fig. 3.13 shows two examples of fibers that were processed in this way. Although this is a more straightforward approach than parallel alignment, since it only requires one milling step with a depth which is the difference between the fiber diameter and the width of the five holes, due to restrictions on the positioning system it is not always possible to align the beam with all holes. For example, while holes in fiber 3.13 (a) were already aligned with the beam, the same was not true in fiber (b) and the positioning system did not have enough amplitude on its degrees of freedom to allow correct alignment. Therefore, this procedure was not further explored since it relied in the uncertain chance that the initial manual fixing of the fiber on the sample holder positioned it in such a way that alignment with the ion beam was possible. Also noteworthy are the broken walls observable in 3.13 (a). This sample originated from fiber 661b2 and it was this observation that ultimately lead to putting this fiber aside.

Finally, an intermediate approach was pursued for inner wall milling. After building the outer channels through polishing with parallel alignment, the fiber was positioned

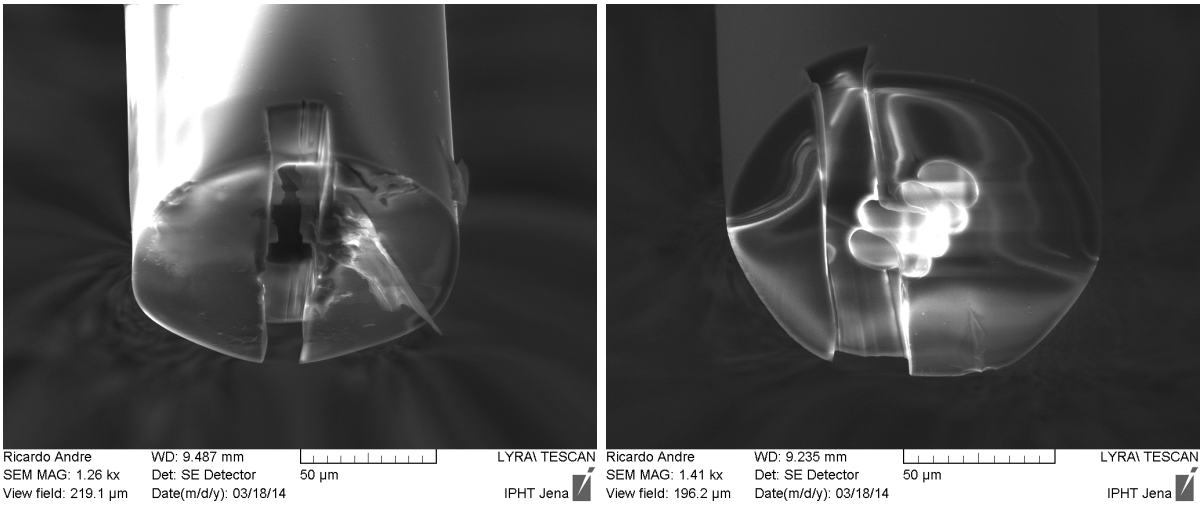

(a) (b)

Figure 3.13: SEM images of MOFs processed with perpendicular fiber-FIB alignment.

at a small angle in relation to the ion beam. This way it is possible to mill the inner walls without weakening the remaining wall structure, as in fig. 3.12 (b). The results of this procedure are displayed in fig. 3.14 and are in general satisfactory. Since it was not possible to precisely control the milling depth so that only one wall is removed with each step, a shadow effect appears in subsequent walls, as seen in fig. 3.14 (a), i.e., after milling a particular wall, if the ion beam is not immediately stopped it will start removing silica from the next one. Nevertheless this can be easily and quickly corrected with additional

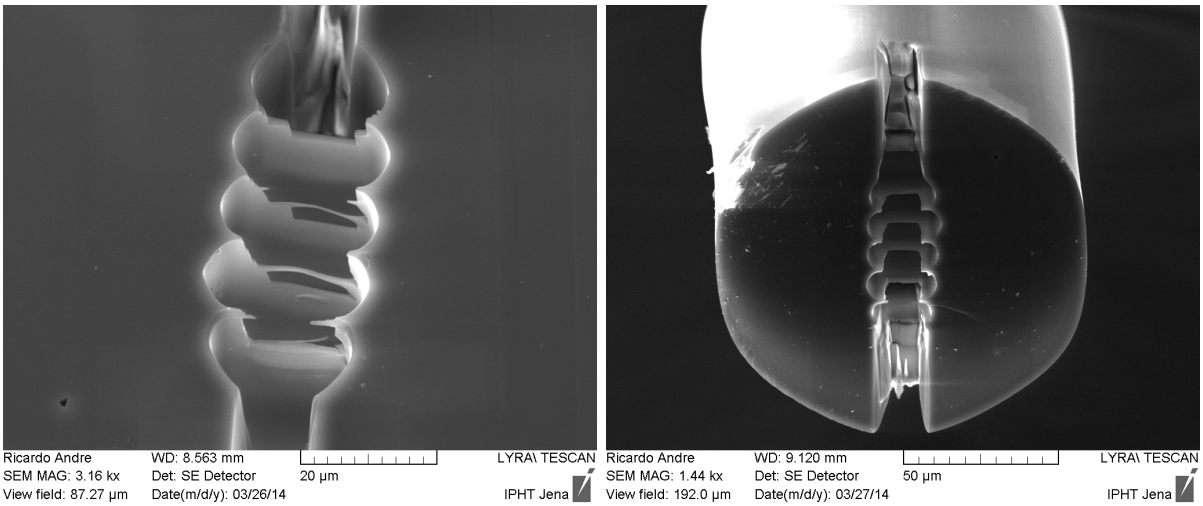

(a) (b)

Figure 3.14: SEM images of MOFs processed with a small fiber-FIB angle for inner wall milling.

milling steps as in fig. 3.14 (b).

To conclude, from these tests it was observed that the best approach for efficient fiber processing would be to polish the outer channels from outside in with parallel alignment, and to mill the inner walls with a small fiber-FIB angle. Milling a whole MOF tip takes between 90 min to 120 min, depending on the level of additional steps to correct redeposition effects and imperfections. However, manufacturing a complete sensing head takes much more time since this needs FIB processing on both ends, which implies at least two sputtering phases and splicing to SMFs that brings added risks to the entire process, as described in the following section.

3.7 Sensor splicing

As mentioned previously, the 5-hole MOF proved to be particularly difficult to handle due to its frailty. Indeed, all sensor manufacturing steps required special care: uncoating, gluing and ungluing fibers to and from FIB holders, placing holders on the sputtering chamber, cleaving and splicing. A large fraction of processed fibers eventually broke in one of these steps. Consequently, only a very small number of sensing heads survived: one was successfully processed and spliced on both ends, as in fig. 3.7 (c), and two were processed and spliced only on one end.

Fig. 3.15 shows two different examples of SMF-MOF splices in which the MOF tips

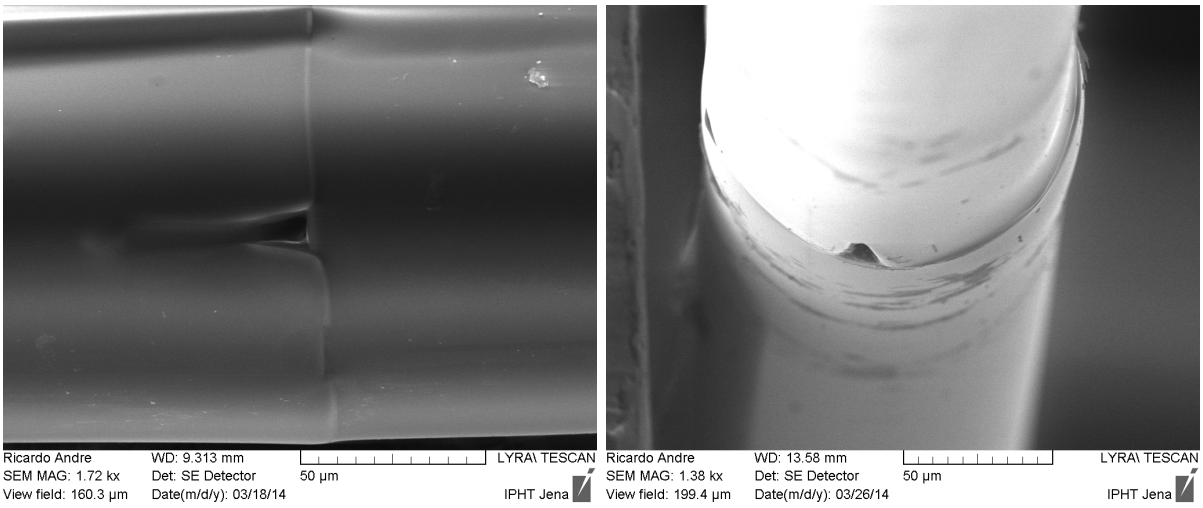

(a) (b)

Figure 3.15: SEM images of spliced MOFs previously processed with microchannels.

were previously processed with the FIB. Although it was not possible to observe the structure internally, the outer channels seem to be intact from the splicing process, which may lead to the conclusion that there is no total collapse of the microfluidic channels. By submerging the sensing heads in acetone it was possible to fill the inner holes completely without the formation of air bubbles. The same was true when submerging in RI oil, although approximately 1 h was necessary for the air bubbles to leave the holes. These small experiments constitute further evidence of post-splicing microchannel structural integrity.

3.8 Conclusion

In summary, a five-hole caterpillar-like microstructured optical fiber was fabricated using a stack-and-draw procedure. Starting with a $\sim$ 13 mm glass preform, the drawn fiber had an average diameter of 120 μm. Its inner holes were approximately rectangular, 11 μm-wide and 22 μm-high, and they were separated by thin 0.3 μm-thick walls.

Several fiber samples were placed on a focused ion beam in order to create microfluidic channels on both cleaved ends to allow fluid inflow after the fiber is spliced to standard single-mode fibers. After several tests it was observed that the best approach for efficient fiber processing appears to be the polishing of the outer channels from outside in with parallel alignment, and the milling of the inner walls with a small fiber-FIB alignment angle. A high FIB current was used since the post-processing steps do not require high-resolution milling, which can be advantageous for quick industrial fabrication of sensing heads using the present methodology.

Although this caterpillar MOF was difficult to handle and most sensor samples broke during the manufacturing process, three sensing heads were successfully produced: one was processed and spliced on both ends, and two were processed and spliced only on one end.

Future work should include the sensor's characterization in terms of propagation properties, a study of the ability to fill and empty the sensor at will, and research on the sensing head's capabilities for fluid sensing. As an example, preliminary simulations predict that when the holes are filled with a fluid with an RI higher than that of SiO_2, light inside each hole is coupled by the thin fiber walls and interference effects occur as a function of

fiber length and the fluid's RI. This behaviour could be studied with the manufactured sensing heads by analysing the fiber's output field when filled with different RI fluids, potentially leading to an RI interferometric sensor based on advanced techniques which enable easier fluid filling. This prospective line of research could thus be interesting both from a fundamental and practical approach.

Chapter 4

Evaporation of Volatile Compounds in Suspended-Core Fibers

4.1 Introduction

Volatile Organic Compounds (VOCs) are substances which are commonly found in many chemical processes, from food and household products to fossil fuels and the chemical industry in general [50]. Some examples are methane, ethanol, acetone and isopropanol. Due to their ubiquitousness, VOC sensors are highly sought devices, although the interest on detecting these substances is motivated mainly due to them constituting serious fire and health hazards. VOCs are highly flammable and can be the source of serious health issues such as cancer. Thus, the need for detecting these compounds either for safety issues or industrial process control is very high.

Since they are flammable, care must be taken when using electronic sensors which may ignite fires or explosions in high concentration environments. In this matter, optical fibers have the obvious advantage of being light-based, eliminating the risk of combustion ignition. Also, since optical fiber sensing setups are usually simpler than electronic ones, they are easier to integrate in critical applications where VOC sensing is needed. The use of optical fiber sensors for VOCs has been reviewed in [50]. These follow the general principles already presented in section 2.1: extrinsic sensors based on spectroscopic measurements of the gaseous environment, evanescent field enhanced interactions (using tapers, bending or Long Period Gratings), fluorescence detection or optrode-like coated fiber tips. Most of these configurations use Single Mode Fibers (SMFs), mainly since this

is a mature technology and the potential that Microstructured Optical Fibers (MOFs) can have in this area has only recently started to be explored.

4.2 Volatile Compound Microstructured Fiber Sensors

One of the possible approaches to VOC sensing using MOFs is to allow the flow of gases inside the fiber holes and measure absorption properties of the environment [11]. In this regard hollow-core fibers are the object of much attention due to their large hole power fractions, although, as mentioned previously, they have much more complicated fabrication procedures than total internal reflection MOFs.

MOF interferometers for refractive index (RI) measurements have also been employed in VOC sensing, such as a Mach-Zehnder in which cladding modes sense changes in the functionalized outer surface of the fiber, or modal interferometers in which the interference between two core modes gives readings of the RI inside the holes of a Photonic Crystal Fiber [51].

Research efforts have been put in VOC gas sensors, specially since there is a big market for tracking the concentration of these gases in several human environments. Notwithstanding, these sensors rely on the diffusion of gases inside fiber holes which is a time-consuming process and in some applications, faster response times are needed. Although in this case RI liquid sensors may be employed, a different approach can be taken by acknowledging that VOCs have high vapour pressures and, consequently, evaporate quickly in ambient temperature and pressure conditions. This fact, in combination with other fluid mechanical characteristics, can be harnessed to build VOC sensors based on the evaporation dynamics of VOC liquids.

Optical fibers have been used for evaporation monitoring either as simple cantilevers [52] or drop holders in spectrometry configurations [53]. The evaporation of droplets has also been analysed using the Fabry-Perot cavity that is formed when a fluid droplet is placed on an SMF tip, between the fiber–droplet and droplet–air interfaces [54]. Laser light reflected on the fiber tip shows intensity oscillations with time due to variations of the Fabry-Perot cavity length caused by the evaporation of the droplet. By tracking the duration of the evaporation process and the number of fringes and through advanced signal processing it was possible to build a sensor capable of distinguishing several VOCs,

after coating the fiber tip with a hidrophobic monolayer.

Recently, a new technique in microstructured fibers for liquid VOC sensing was introduced [55]. Using in-line 100 μm-long microcavities etched in single-mode fibers (Fig. 4.1 (a)), the monitoring of the evaporation dynamics of volatile organic compounds was proposed as a means to identify them. The evaporation of ethanol, hexane, acetone, and a mixture of ethanol and hexane was tracked by measuring light transmitted through the microcavity (Fig. 4.1 (b)), showing clear distinctions in light loss dynamics which effectively results in a volatile compound sensor. With a few assumptions, it was possible to simulate the sensor's behaviour using ray-tracing and wave-propagation analysis. Both resulted in very good agreement with experimental results. Also, the behaviour of a mixture of volatile organic compounds was distinguishable from its individual constituents. This could be used in a laboratory to quickly identify mixtures of substances requiring only small sample volumes.

The previous experiment could in principle be extended to the holes in MOFs with changes in the physical analysis. While in the case of microcavities light crosses the liquid droplet and signal changes are caused by refraction of the guided mode, in MOFs light would interact mainly through the evanescent field, causing much smaller signal variations. This would imply a different interpretation of the phenomenon. However, this work is yet to be discussed in the literature and no references of evaporation monitoring using MOFs was found. MOFs have relevant practical advantages in comparison with microcavities, namely, they are easier and cheaper to fabricate and they are much more robust (microcavities are particularly fragile).

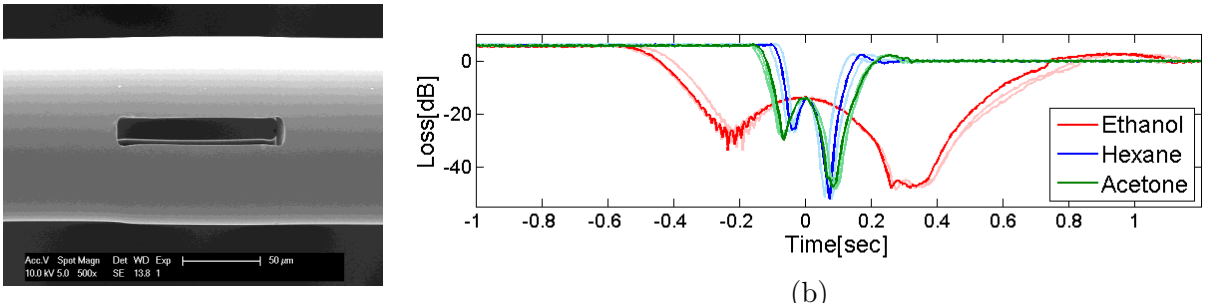

(a) (b)

Figure 4.1: (a) A microcavity etched in a single mode fiber was used to measure the evaporation dynamics of several volatile organic compounds. **(b)** Plot of the transmitted signal loss vs. time with which it was possible to distinguish between ethanol, hexane and acetone. Figures reproduced from [55].

4.3 Suspended-Core Fibers

For the purpose of fluid evaporation monitoring, MOFs with higher hole power fractions would be preferable since they enable higher interaction with liquids in holes without requiring long fiber lengths, maintaining the advantage of small sample volumes of microcavities. In particular, a special class of TIR MOFs called Suspended-Core Fibers (SCFs) are characterized by their nanowire-like small diameter cores held by thin struts in the middle of large air holes [56]. By reducing the core size and the supporting struts' thickness, an increasing fraction of the core guided mode protrudes into the air holes. Light can then strongly interact with fluids that are inserted into these holes and sensing can be performed without the characteristic frailty of thin nanowires and with large hole power fractions [57].

Fig. 4.2 (a) shows the first SCF, proposed and realized respectively in 1999 [58] and 2001 [16], based on the idea of reducing the strut thickness of the first MOF (Fig. 3.1 (a)). For thicknesses lower than the operating wavelength, an increase of the hole power fraction is observed. The first suspended-core fiber had a hole power fraction of 17% at 1550 nm [16].

Since then, suspended-core fibers developed into a prolific research area. This was partially due to their ease of fabrication which gives them a competitive advantage when planning for industrial applications [15]. In fact, it was shown that one can fabricate a suspended-core fiber simply by mechanical drilling of a preform, removing the added

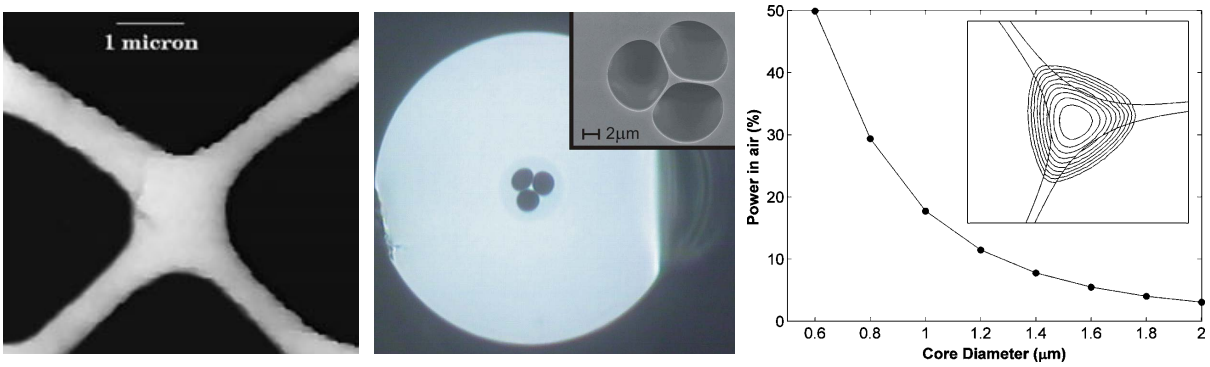

(a) (b) (c)

Figure 4.2: (a) The first report of a suspended-core fiber. Figure reproduced from [16]. **(b)** Three-hole suspended-core fiber fabricated through mechanical drilling of a preform, with detailed picture of the core (inset) and **(c)** simulation results of the hole power fraction as a function of core diameter. Figures reproduced from [57].

complexity of capillary stacking [57]. Figure 4.2 (b) shows an optical microscope picture of the first three-hole SCF fabricated by drawing of a mechanically drilled preform as well as a detailed scanning-electron microscope of the core region. SCFs with core diameters ranging from 0.8 to 1.8 μm where fabricated from this preform and finite element simulations where performed to determine the hole power fraction as a function of core diameter (Fig. 4.2 (c)). As mentioned previously, protrusion of the guided mode into the fiber holes increases for smaller core diameters. This subject is detailed in [56]. Thus, for smaller core diameters, suspended-core fibers become increasingly competitive with hollow-core fibers in terms of hole power fraction and, consequently, equivalent free-space propagation length.

Suspended-core fibers have been used to measure physical parameters [33], for Raman and fluorescence spectroscopy [33, 56], and in biological and chemical sensing. In particular, measurements of liquids have been performed either by effective RI changes in interferometric setups or by absorption spectrum analysis [59]. The large air-holes that characterize suspended-core fibers are advantageous in comparison with conventional TIR PCFs since they allow for much lower fluid filling times due to weaker interaction with hole surfaces [16].

4.4 Evaporation Monitoring using SCFs

With the advantages of SCFs in mind, during this dissertation a new approach to VOC fluid evaporation monitoring was proposed based on a suspended-core fiber tip. The basic concept behind this work was to use the holes of an SCF for a similar purpose as microcavities in ref. [55], filling them with VOCs and tracking the evaporation dynamics. The SCF is illuminated by splicing it to an SMF. The other end of the fiber has to remain open to the external environment to allow filling the holes with liquids. As such, the sensing head is interrogated in a reflection geometry.

Fig. 4.3 represents schematically the experimental setup. The sensor was dipped in a VOC reservoir at room temperature and its time-dependent evaporation dynamics were studied. To perform the interrogation, the SMF was connected to an optical circulator. Light was introduced from a 100 nm-wide optical source centered at 1550 nm and the reflected signal was interrogated using an Optical Spectrum Analyser (OSA) with a max-

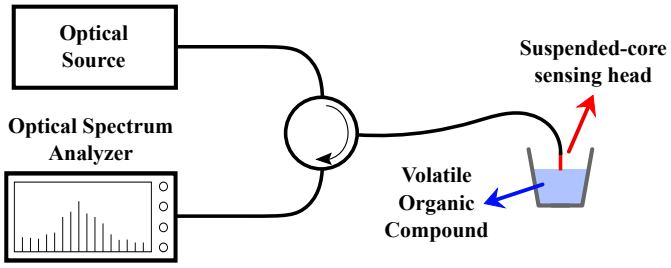

Figure 4.3: Diagram of the experimental configuration used for VOC sensing.

imum resolution of 0.01 nm. An optical microscope was used to observe the phenomenon simultaneously.

Two sensing heads were studied, with differing lengths of the SCF sensing tip: one with $L_1 = (1.38 \pm 0.02)$ mm and the other with $L_2 = (0.33 \pm 0.02)$ mm. At rest, both sensors form Fabry-Pérot cavities due to the reflections on both ends of the SCF: the splice region, and the interface between the SCF and the external environment. Fig. 4.4 shows the spectra of each sensing head when at rest, i.e., when no liquids are present inside the SCF holes. As indicated in the figure, sensor 1 has a $\mathrm{FSR}_1 = (0.61 \pm 0.02)$ nm and sensor 2 has $\mathrm{FSR}_2 = (2.59 \pm 0.02)$ nm. Note that, as expected from eq. 2.1, a smaller cavity length leads to a larger FSR. Also, since FSR, λ and L are measured quantities, from eq. 2.1 it is possible to derive an *effective* RI, n_{eff} for each sensor, respectively $n_{\mathrm{eff},1} = 1.43 \pm 0.05$ and $n_{\mathrm{eff},2} = 1.40 \pm 0.09$. Both values are close to that of fused silica

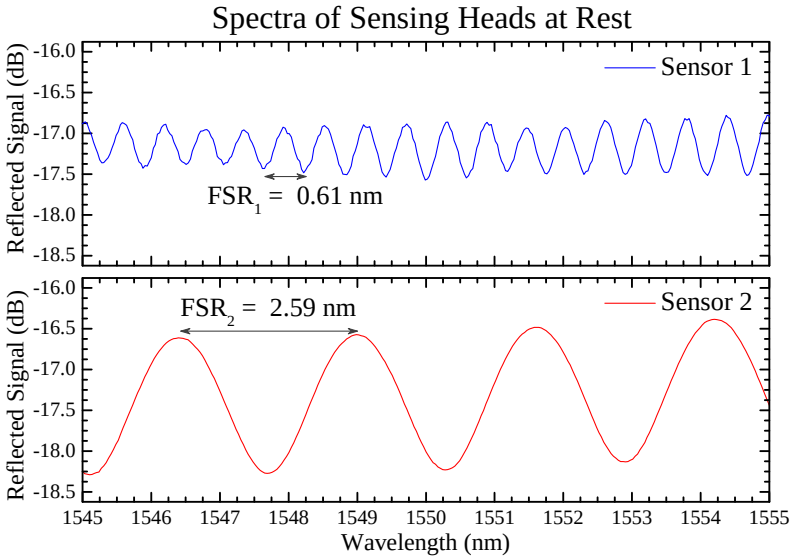

Figure 4.4: Spectra of both sensing heads when at rest. The increase of the free spectral range for shorter sensing heads is visible: sensor 1 has a length of 1.38 mm and sensor 2 is 0.33 mm long.

Table 4.1: Summary of the length of both SCF sensing heads, as well as the free spectral range and effective refractive index of the Fabry-Perot cavities.

Sensor	L (mm)	FSR (nm)	n_{eff}
1	1.38 ± 0.02	0.61 ± 0.02	1.43 ± 0.05
2	0.33 ± 0.02	2.59 ± 0.02	1.40 ± 0.09

$n_{SiO_2} = 1.444$, the most common type of glass used in MOFs [60]. The properties of both sensors are summarized in table 4.1.

Each sensing head was dipped in acetone and isopropyl alcohol but they were studied differently. While in the case of sensor 1 the spectral evolution was analysed broadly, for sensor 2 only a narrow region around $\lambda = 1.55\,\mu$m was observed. Before describing the results of both broad and narrowband studies, the SCF that was used will be presented.

4.5 Double-Y-shaped SCF

In these experiments, an asymmetric four-bridge silica fiber with a double-Y-shaped suspended-core was used. Fig. 4.5 (a) shows an optical microscopy image of the fiber's cross-section, whereas fig. 4.5 (b) shows a magnified SEM image of the region around the core. The fiber's outer diameter is $130\,\mu$m while the diameter of the air-hole cladding is $65\,\mu$m. The supporting struts are $0.9\,\mu$m-thick. The core is approximately rectangular with a length of $10\,\mu$m and a varying width between $1\,\mu$m at the waist and $3.2\,\mu$m near the struts.

This fiber was chosen since an enhancement of the interaction of the evanescent field

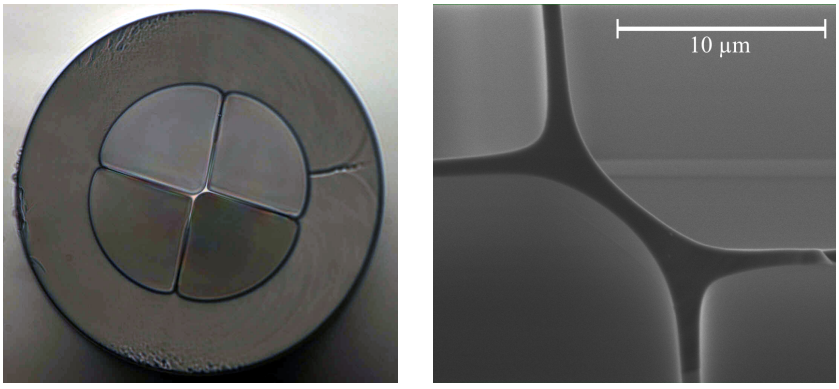

(a) (b)

Figure 4.5: (a) Suspended-core fiber cross-section and **(b)** core region.

with surface effects is expected, due to the fiber having a greater surface area near the core. It should be noticed that due to their high RI contrast, the normalized frequency V of SCFs is usually high, implying multimode operation. For conventional fibers, the V parameter is defined as

$$V = \frac{2\pi}{\lambda} a \sqrt{n_{\text{core}}^2 - n_{\text{cladding}}^2} \tag{4.1}$$

where λ is the light wavelength, a is the core radius and n_{core} and n_{cladding} are respectively the RI of the core and cladding [1]. Considering the example of a fiber with $a = 1\,\mu$m, $n_{\text{core}} = n_{\text{Silica}} \approx 1.44$ and $n_{\text{cladding}} = n_{\text{air}} = 1$, light with $\lambda = 1.55\,\mu$m propagates with $V = 4.2$, a normalized frequency higher than the single-mode cutoff condition of $V < 2.4$. Thus, one sees that even with a small $1\,\mu$m core, the high RI contrast of SCFs make them multimode fibers.

Using COMSOL Multiphysics, a Finite Element Method simulation software, it was possible to obtain the propagating modes of this fiber and their respective hole power fractions. The fiber's cross-section was drawn in AutoCAD, based on the SEM measurements of fig. 4.5 (b), and imported into COMSOL. Fig. 4.6 (a) shows the simulated region of the SCF's core. For the sake of scale comparison, fig. 4.6 (b) shows the cross section of an SMF, which typically has a diameter of $8\,\mu$m, over the SCF. From fig. 4.6 (b) it is also possible to notice that only a small fraction of light from the SMF will couple with the SCF modes due to the small overlap between both cores. In fact, as mentioned in section 3.3, one of the biggest loss mechanisms in coupling light from an SMF to an MOF is mode field mismatch, a problem that is clearly observable with SCFs.

Fig. 4.7 shows the average power in the propagation direction of some modes, whereas

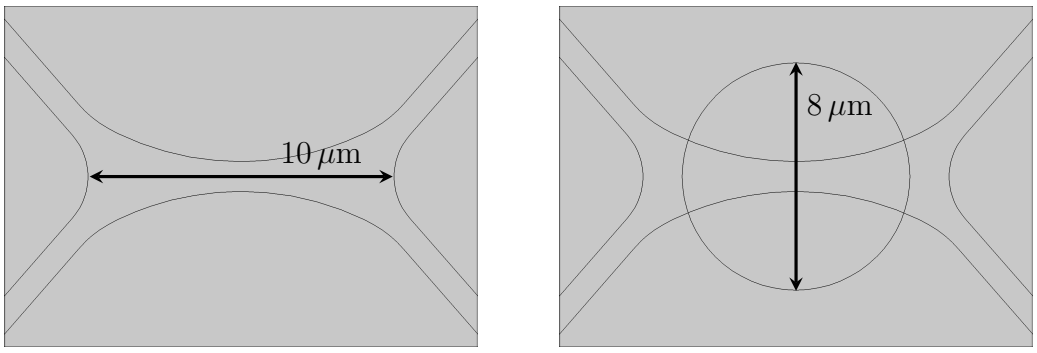

Figure 4.6: **(a)** Drawing of the SCF cross section region that was simulated. **(b)** Cross section of an SMF's core over the SCF for scale comparison.

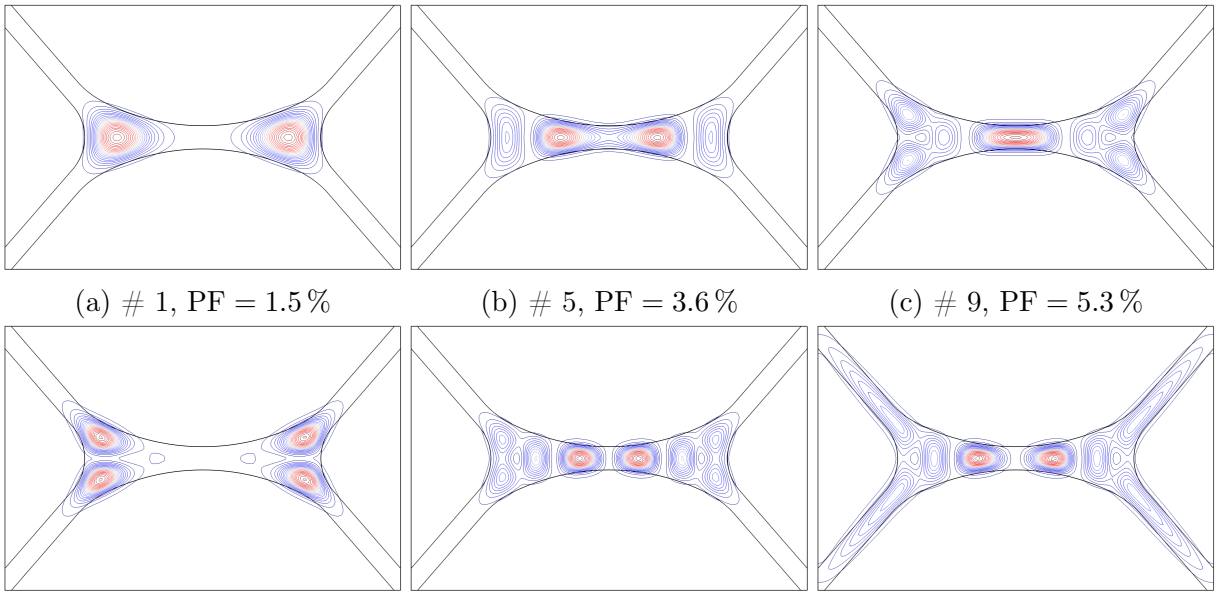

(a) # 1, PF = 1.5 % (b) # 5, PF = 3.6 % (c) # 9, PF = 5.3 %

(d) # 10, PF = 4.27 % (e) # 14, PF = 4.1 % (f) # 16, PF = 6.9 %

Figure 4.7: Simulation results of the average power in the propagation direction of a selection of the first simulated modes. Figure captions indicate the mode order number (#) and its hole power fraction (PF).

table 4.2 indicates the hole power fraction for each mode and its corresponding effective RI. It is possible to see that higher order modes have in general higher hole power fractions. Intuitively this behaviour is interpreted in a simplified way by the broadening of modes with increasing order and the consequent increase of energy that propagates evanescently through the holes. Thus, if one thinks of the effective RI as a weighted average of the indices through which light propagates, it is as if modes are increasingly affected by the holes' RI when they are broadened, resulting in lower effective RIs.

In particular, from the simulation results one observes that modes 1 through 4 are highly confined on both ends of the core's concave structure, similar to a double core fiber, showing smaller hole power fractions. Higher order modes become increasingly protruded and from mode 16 onwards, a larger fraction of energy propagates through the SCF struts. Since these have smaller dimensions than the core, modes are broader and consequently have higher hole power fractions.

Notice that both sensing heads have effective RIs close to 1.4 (table 4.1), indicating that most light propagates through the fused silica core and that the hole power fraction may be similar to that of the lower propagating modes. Notice also that the hole power fractions obtained through COMSOL are in agreement to that of the ones of fig. 4.2 (c)

Table 4.2: Simulation results of the effective refractive index (n_{eff}) and hole power fraction (PF) of the first propagation modes.

#	n_{eff}	PF (%)	#	n_{eff}	PF (%)
1	1.40562	1.5	11	1.35058	4.26
2	1.4056	1.49	12	1.349	4.5
3	1.403411	1.339	13	1.346	4.4
4	1.4034108	1.338	14	1.335	4.1
5	1.374	3.6	15	1.332	5.5
6	1.372	3.2	16	1.328	6.9
7	1.3654	2.8	17	1.326	10.3
8	1.3651	2.77	18	1.3253	10.7
9	1.352	5.3	19	1.3252	10.3
10	1.3506	4.27	20	1.324	8.7

in terms of orders of magnitude, even though the cross-section of both fibers is different. For example, the first modes, highly confined in regions with an average width of 2 μm, have very low hole power fractions, whereas higher modes that propagate largely through the thin 0.9 μm struts show power fractions an order of magnitude higher.

4.6 Spectral Analysis

The time-dependent spectral response of sensing head 1 was coarsely monitored when its cavities were filled with acetone. A broadband spectral analysis should allow the observation of changes in the Fabry-Perot cavity and of spectral phase shifts that may occur during the evaporation process. The sensor was studied when a droplet with a few tens of microliters of acetone was dispensed with a syringe on the open end of the suspended-core fiber.

Figure 4.8 contains a series of microscope pictures that show the evolution of acetone evaporation from sensing head 1. When acetone is dispensed on a clean (fig. 4.8 (a)) sensing head the air-holes are filled by capillarity forces and excess liquid that surrounds the fiber tip (fig.4.8 (b)) rapidly evaporates. As soon as the acetone that covers the tip evaporates, four menisci form (fig. (c)) inside each individual cavity. For clarity, arrows indicate the position of each meniscus. Each hole appears to have different evaporation rates and some seconds after the formation of all menisci, the differences in position among them become clearer, as seen in fig. (d), 12 s after the beginning of this process.

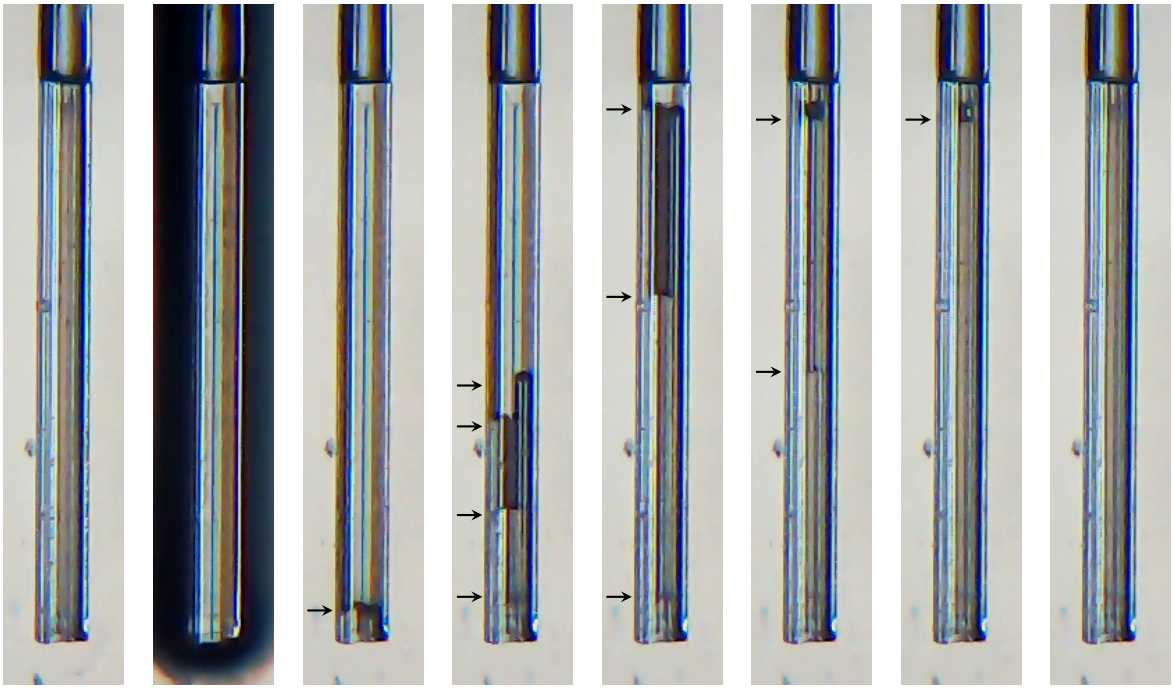

(a) (b) (c) (d) (e) (f) (g) (h)

Figure 4.8: Evolution of acetone evaporation from sensing head 1 since before dispensing acetone **(a)** until the evaporation process is over **(h)**. Arrows indicate the positions of menisci.

When the acetone in an individual cavity evaporates completely, its meniscus collapses. Due to the different evaporation rates, this happens sequentially. Each meniscus is shown immediately before collapse: in fig. 4.8 (e) the first two collapse almost at the same time, 31 s and 35 s after evaporation starts; in fig. 4.8 (f) the third, after 46 s; and in fig. 4.8 (g) the fourth, after 61 s. The whole process takes about 1 min since evaporation of acetone inside the SCF cavities starts and in the end (fig. 4.8 (h)) one observes that the fiber restores its rest condition.

After repeating the experiment one notices that the evaporation dynamics depend on the way acetone fills the cavities. Air bubbles often form inside the holes which cause differences in evaporation rates and total duration. Also, the fiber was filled with acetone while in contact with a microscope slide, which may be the source of additional degrees of freedom that alter the way fluids start evaporating on the SCF holes.

The sensing head that was used shows an average evaporation time of ~ 45 s, a value that certainly depends on fiber length. Although with different geometries, one can verify the time dependency on length by comparing our ~ 1.4 mm length fiber with the microcell from ref. [55], which had a cavity length of 100 μm and a total evaporation time of ~ 0.5 s

for acetone.

During the study of evaporation dynamics, the sensing head was continuously interrogated using an OSA. The OSA's slow sampling time resulted in a small time resolution of ±4 s. Still, as mentioned in the previous paragraph, the total evaporation time was an order of magnitude higher than this, which allowed for a coarse spectral analysis of the phenomenon.

The data acquired is plotted in Fig. 4.9. As already mentioned, at rest a Fabry-Perot interferometer spectrum can be seen, with a visibility[1] of 0.6 dB and a period of (0.61 ± 0.02) nm, constant throughout the whole process. Figure 4.9 (a) shows the spectrum at rest, before acetone is dispensed. When the sensor is immersed in acetone (fig. 4.9 (b)) intensity drops 14 dB and the cavity disappears almost completely due to the higher refractive index of acetone (~ 1.36) in comparison with air and the consequent reflectivity decrease on the fiber tip. When acetone surrounding the sensor evaporates and menisci start to form, visibility grows to 6.3 dB as observed in fig. 4.9 (c) since initial reflectivity values at the tip are restored, although the average intensity is still lower than at rest. As acetone inside the cavities evaporates, visibility decreases. Figure 4.9 (d) has an amplitude of 4.5 dB. The spectrum returns to its initial average intensity after the first meniscus collapse. From then until the end of evaporation, the spectrum retains the same average intensity, suffering only a spectral phase shift (fig. 4.9 (f)) which may arise from dust flowing inside the SCF during acetone dispensing due to it being in contact with the microscope slide.

Due to the large scanning time of the OSA, using this methodology the evaporation dynamics are largely undersampled and it is not possible to observe all changes the spectrum suffers. Moreover, repeatability of the experimental results could not be achieved, mainly due to the difficulty in synchronizing OSA sampling with the evaporation process but also because it was not possible to fill the holes always in a homogenous manner. For example, the formation of air bubbles inside the fiber holes imposes a strong limitation on repeatability. Also, the fiber should avoid contact with the microscope slide in order to reduce external influences.

Notwithstanding, with this experiment the general behaviour of this sensor was observed. The sensing head forms a Fabry-Perot cavity that maintains its spectral shape

[1] Difference between maximum and minimum intensity.

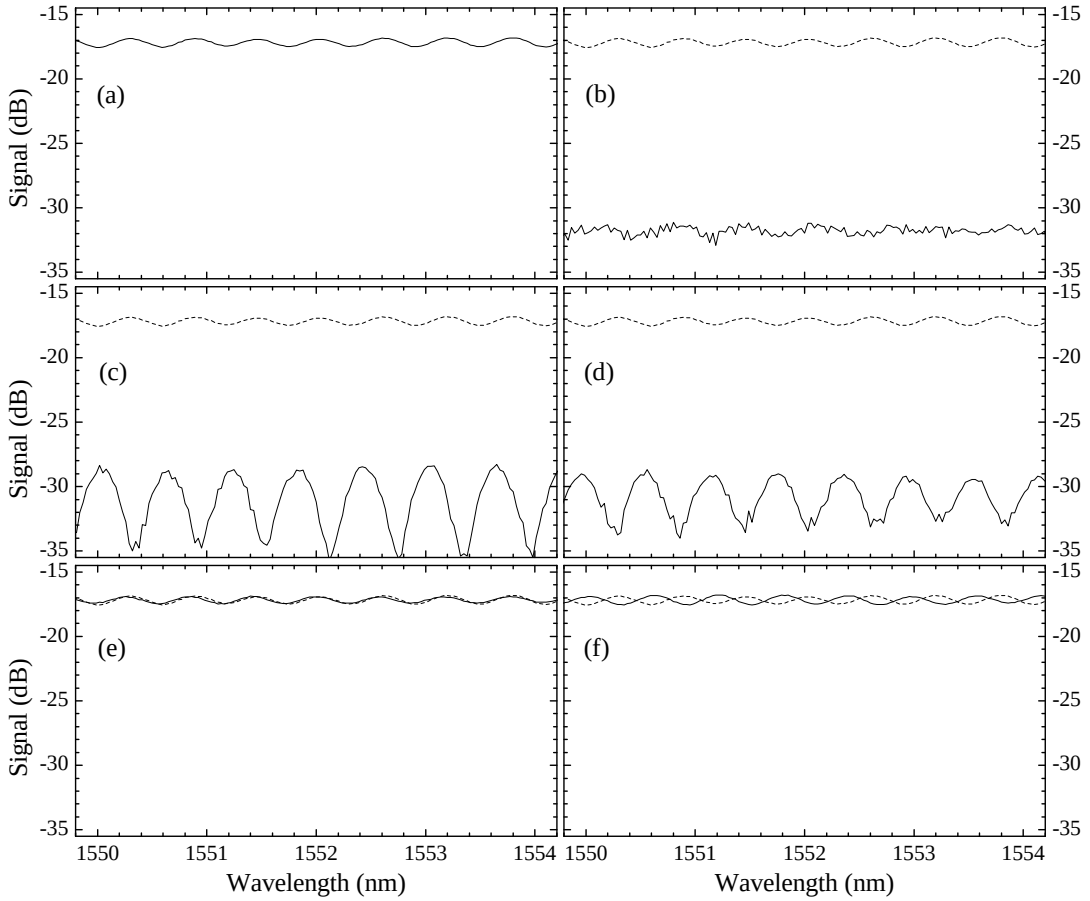

Figure 4.9: Spectral evolution measured with reference to the optical source since before dispensing acetone **(a)** until the evaporation process is over **(f)**. For ease of comparison, data from **(a)** is repeatedly plotted as a dashed line.

throughout most of the process, with the exception of when the SCF is submerged in acetone. Contrary to what would be expected, the spectrum returned to the initial state after the collapse of the first meniscus (Fig. 4.8 (e) and 4.9 (e)), suggesting that there is a dominant cavity and that not all of them have a similar contribution to the overall behaviour. However, this experimental procedure did not allow a more detailed analysis of the phenomenon. The narrowband intensity analysis described on the following section allowed for further investigations of this sensing configuration.

4.7 Intensity Analysis

In order to solve the repeatability problem of the broadband analysis, using a shorter sensing head should lead to a more uniform filling of the cavities. For this, sensor 2 was used, with length $L_2 = (0.33 \pm 0.02)\,\mathrm{mm}$. A shorter sensor also has faster dynamics

since the amount of liquids involved is smaller, thus requiring faster interrogation times. The sampling problem can be overcome by measuring only the reflected signal of a single wavelength, i.e., of a narrow band around a specific wavelength. For this, $\lambda = 1.55\,\mu$m was chosen since it is a commonly used wavelength in telecommunications, consequently having the cheapest available equipment, an important factor to consider for future potential industrial applications. Also in an effort to improve repeatability, the sensor was slightly elevated from the microscope slide to reduce its influence on the filling and evaporation processes.

Figure 4.10 displays the evaporation process of acetone as observed through the optical microscope. The most striking difference from sensor 1 is that apparently only one menisicus moves throughout most of the process. Figure 4.11 shows measurements of the sensing head's reflected signal as a function of time after dipping in acetone and isopropyl alcohol (IPA). Three different measurements are displayed for each substance, which shows the reproducibility of results.

In order to synchronize all measurements, a possible approach would be to consider the first signal drop as the beginning of the process, i.e., right when the sensing head is dipped in the corresponding substance. However, two problems arise. First, the dipping process was performed manually. Consequently, perfect reproducibility of the time during which the sensing head is immersed in liquid could not be guaranteed, causing delay differences until the beginning of the actual evaporation process. Secondly, after dipping, different amounts of liquid surround the fiber tip through the formation of a droplet around the sensing head. The evaporation of this droplet can be tracked with our sensor and it is also associated with reduced reproducibility. As such, all measurements where synchronized

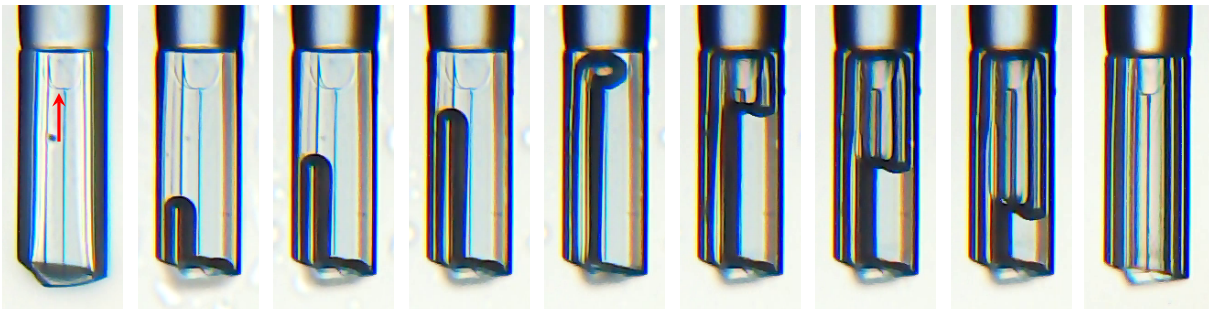

Figure 4.10: Evolution of menisci position inside the sensing head during the process of acetone evaporation. The red arrow indicates the location of the structure's collapse.

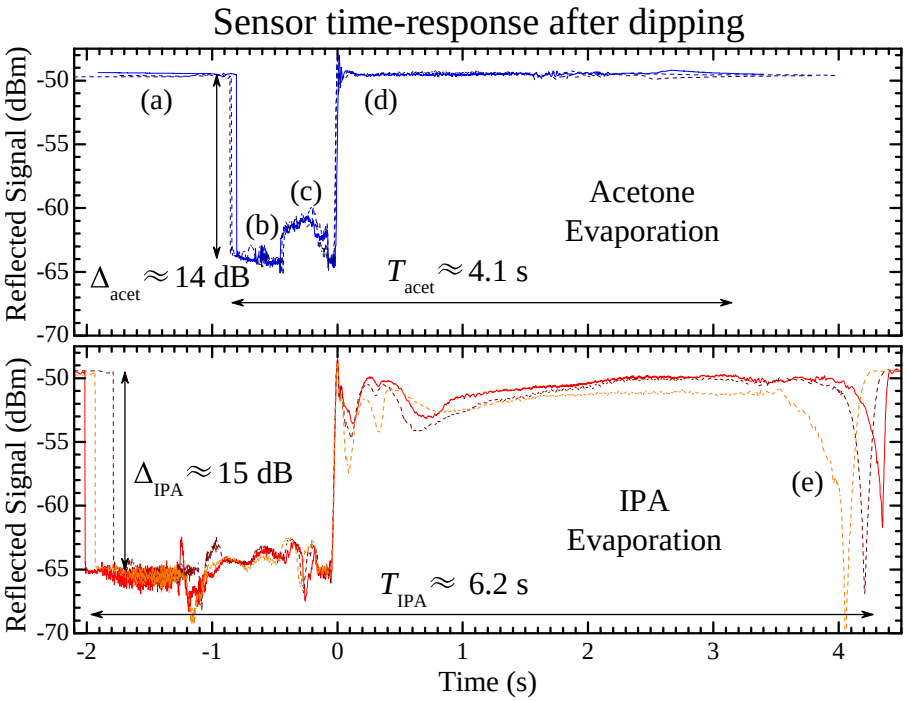

Figure 4.11: Sensor time-response after dipping in acetone and IPA. Three different measurements are shown for each substance. The letters in parenthesis indicate different evaporation phases.

by setting the most abrupt signal increase as $t = 0\,\mathrm{s}$, as seen in fig. 4.11.

From fig. 4.11 one can observe that although both substances show overall similar evaporation behaviour, there exist strong differences that allow their differentiation, namely the signals' duration and oscillations before and after $t = 0\,\mathrm{s}$. The process duration is defined as the time it takes for the signal to restore its rest condition after being

Table 4.3: Estimated reflectivities for each evaporation phase. Correspondence of each phase is made with other figures. Where two values appear, they correspond to acetone and IPA, respectively.

Phase	Empty	Submerged	Bottom full	Bottom empty
R_1 (%)	3.4	0.1/0.06	0.1/0.06	3.4
R_2 (%)	2.8	0.02/0.005	0.02/0.005	2.8
R_3 (%)	2.8	0.02/0.005	2.8	2.8
Fig. 4.8	(a,h)	(b)	(c,d)	(e,f,g)
Fig. 4.9	(a)	(b)	(c,d)	(e,f)
Fig. 4.10	(i)	(a)	(b,c,d)	(e,f,g,h)
Fig. 4.11	(a)	(b)	(c)	(d)
Fig. 4.12	(a)	(b)	(c)	(d)
Fig. 4.13	(e)	–	(b)	(c,d)

dipped in a volatile compound, i.e., until signal oscillations due to fluid evaporation are not detected. With this definition, acetone evaporation takes an average of $T_{\text{acet}} \approx 4.1\,\text{s}$ with only minor oscillations after $t = 0\,\text{s}$, while IPA takes an average of $T_{\text{IPA}} \approx 6.2\,\text{s}$ with stronger oscillations after $t = 0\,\text{s}$ than acetone.

One common feature in the evaporation of both substances is the existence of *high* and *low* signal states with strong intensity differences Δ between them. In particular, $\Delta_{\text{acet}} \approx 14\,\text{dB}$ and $\Delta_{\text{IPA}} \approx 15\,\text{dB}$. In comparison with the results of fig. 4.9 from sensor 1, the high state corresponds to the situations in which the average intensity is higher, and the low state to those in which the average intensity drops.

In order to interpret the origin of these values it is necessary to observe the structure of the fabricated sensor in closer detail. The red arrow in fig. 4.10 (a) indicates the presence of a defect in the SCF close to the spliced region. This corresponds to a collapse of the SCF structure due to the splicing process that lead to the creation of connections between the fiber holes. Further evidence of this comes from observation of the evaporation process through fig. 4.10. It can be seen that in this experimental instance an air-acetone meniscus forms in one of the holes (fig. 4.10 (b)) and starts propagating from the outside in. As it reaches the collapsed region (fig. 4.10 (e)), the first meniscus divides itself into three others in the remaining holes holes, and propagation proceeds from inside out until all acetone evaporates and the sensor returns to its initial state (fig. 4.10 (i)).

The sensor structure is schematically represented in fig. 4.12 (a). Close to the spliced region, on the SCF's bottom, the structure collapse is modelled through a gap in the SCF core. The RIs of the SMF propagating mode $n_{\text{SMF}} \approx 1.45$ and of the fused silica SCF core $n_{\text{SCF}} \approx n_{\text{eff},2} = 1.40 \pm 0.09$ can be considered constant throughout the sensing process, as a first order approximation. However, both the RIs inside the SCF holes n_{in} and outside the sensing head n_{out} can take the values of $n_{\text{air}} \approx 1$ when empty or $n_{\text{acet}} \approx 1.36$ or $n_{\text{IPA}} \approx 1.38$ when filled with acetone or IPA respectively.

With these refractive indices, three main reflections R can be defined by Fresnel's equations: $R_1 = \left((n_{\text{SMF}} - n_{\text{in}})/(n_{\text{SMF}} + n_{\text{in}})\right)^2$ on the interface between the SMF and the SCF collapsed region, $R_2 = \left((n_{\text{in}} - n_{\text{SCF}})/(n_{\text{in}} + n_{\text{SCF}})\right)^2$ between the collapsed region and the SCF core and $R_3 = \left((n_{\text{SCF}} - n_{\text{out}})/(n_{\text{SCF}} + n_{\text{out}})\right)^2$ between the SCF core and the external environment. An overall interpretation of the sensor's time-response can be obtained with an analysis of the evolution of these reflections. The evaporation process

can be divided into four different phases, represented by the four images in fig. 4.12. The corresponding reflectivities are indicated in table 4.3 and were calculated without considering the effective RI changes of the SCF when the holes are filled with acetone or IPA.

Before dipping (phase Empty) all reflections have high values and light does not interact with any fluid. This translates in a high stable value as seen in fig. 4.11. Immediately after dipping (phase Submerged), most light couples to the external environment and a strong signal drop Δ is observed. Considering only the changes in R_1 between phases Bottom full and Bottom empty, one would expect signal drops of the order of $10\log_{10}\left(\frac{3.4}{0.1}\right) \approx 15.3\,\text{dB}$ for acetone and $10\log_{10}\left(\frac{3.4}{0.06}\right) \approx 17.5\,\text{dB}$ for IPA. These values are similar to the measured Δ's and the small differences between them may be due to our simplistic calculation that just considers light reflected at the interface and ignores back propagating light reflected at R_2 and R_3 as well as coupling losses between the SMF and the SCF. When acetone from the collapsed region evaporates, between phases Bottom full and Bottom empty, the signal returns to the high state, since reflection values also return to the initial states.

Table 4.3 also makes a correspondence between each evaporation phase and other figures shown. In particular, comparing fig. 4.9 with the reflectivity values on the table, one sees that while on the low state, the Fabry-Perot cavity spectrum returns when the fluid that surrounds the sensing head evaporates and the reflectivity R_3 of the SCF tip recovers its original value. During the phases before and after fluid on the SCF's

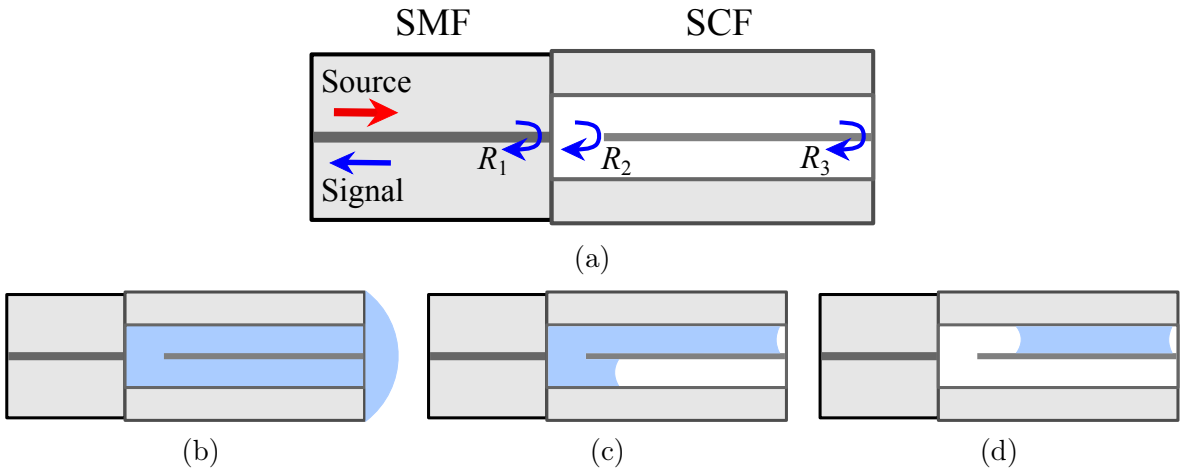

Figure 4.12: Scheme of the sensor structure **(a)** and of the main evaporation phases **(b)**–**(d)**.

bottom evaporates, fig.s 4.12 (c) and (d), smaller signal oscillations are observed. These may originate from spectral phase oscillations caused by the interaction between the evanescent field and remaining acetone inside the SCF holes that change the effective RI and, consequently, the phase of the Fabry-Perot cavity, or due to temperature variations from the endothermal evaporation process, since the sensing head was found to have a temperature sensitivity of (12.16 ± 0.09) pm/°C (adjusted $r^2 = 0.998$) in the range from 20 °C to 100 °C.

It should be noted that although in the case of acetone the sensor seems to quickly recover to the initial state immediately after the evaporation of the collapsed region, the same does not apply for IPA. In fact, several signal variations are observable for $t > 0$, most noticeably the strong dip at the end of evaporation (fig. 4.11 (e)). These differences can be attributed to other material properties, such as viscosity, which condition the way menisci move inside the holes and, consequently, how the fluid is positioned throughout evaporation, as seen in fig. 4.13. In the case of IPA it appears that when the first meniscus reaches the collapsed region, the others start propagating from outside in, contrary to what happens with acetone. As a result, some remaining IPA interferes with the collapsed region before the end of evaporation, provoking the observed signal drop.

4.8 Conclusion

To conclude, two sensing heads comprised of a four-bridge Suspended-Core microstructured fibre tip, fusion-spliced to a standard single-mode fiber, were immersed in acetone and isopropanol and the evaporation dynamics of each fluid were simultaneously analysed

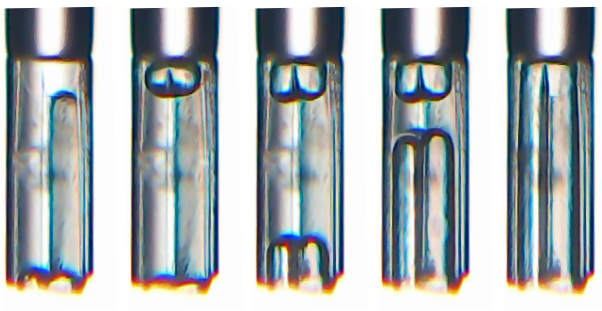

(a) (b) (c) (d) (e)

Figure 4.13: Evolution of menisci position inside the sensing head during the process of IPA evaporation.

with an optical microscope and an Optical Spectrum Analyser. Near the splice, the microstructured fiber is collapsed due to the electric-arc fusion process, which deforms the SCF structure, possibly damaging both core and struts, creating microfluidic channels between the fiber holes.

The time-dependent behaviour of the sensing heads after being dipped in a volatile compound was characterized using a broadband spectral analysis and an intensity (narrowband) reading. Both approaches lead to different insights on the way this sensor works. A Fabry-Perot cavity formed by the reflections on the splice and sensor tip was observed during most of the process. The signal intensity dynamics and the total signal duration differ between acetone and IPA. These can be considered signatures of each fluid's evaporation properties, directly related to their chemical composition and interactions with the environment. Strong signal variations seem to be related to reflectivity changes in the collapsed region, whereas small signal oscillations are attributed to refractive index changes in the evanescent field of the suspended-core fiber propagating modes.

This configuration could thus be used to detect and study the evaporation of different volatile organic compounds. Contrary to spectroscopy applications where long sensing heads are preferred to maximize fluid-light interaction [51], in the case of evaporation monitoring a short sensor tip should be used to maximize experimental repeatability, reducing the risk of air bubble formation and facilitating the filling process. Shorter sensors also result in low-volume sensing solutions, which make the proposed configuration useful for industrial or environmental process monitoring. Also, the use of suspended-core fibers as opposed to direct fabrication of micro-cavities in standard single mode fibers makes for sensors with lower cost and easier production and handling.

Finally, although the splicing process was thought to have been optimized to avoid structural collapse, this effect occurred nevertheless. Even though the collapse is only faintly noticeable through optical microscopy, the observation that fluids easily fill the whole cavity is an indication of the existence of microfluidic channels, contrary to what happens in MOFs which are homogeneously sealed on one end. This ultimately became a serendipitous mechanism to fabricate a sensing head optimized for the study of fluids.

Chapter 5

Concluding Remarks and Future Prospects

Throughout this dissertation, a variety of fundamental resources required for performing research work in optical fiber devices was explored. With the constant aim of exploring Microstructured Optical Fibers (MOFs) for fluid sensing applications, this dissertation covered the fabrication of MOFs, the advanced manufacture of MOF-based sensing heads and the study of a particular sensor for Volatile Organic Compounds (VOCs).

First, a 5-hole caterpillar-like MOF was fabricated using a stack-and-draw methodology. This step comprised an understanding of MOF production techniques and also the optimization of drawing parameters for this specific fiber design. The fiber's inner walls between holes have submicrometric thickness which may ease coupling of light between holes through the evanescent field. Although fragile, it was possible to splice this MOF to standard fibers envisaging the future manufacture of sensing heads.

Subsequently, the caterpillar MOF was post-processed using a Focused Ion Beam (FIB). This technique allows for highly detailed tailoring of the fiber structure at a localized level and it was used to create microfluidic channels on the MOF that allow the flow of fluids in and out of the MOF even if it is spliced on both ends to other standard fibers. A methodology was presented to build these microchannels taking into account the positioning limitations of the FIB that was used. Several sensing heads were successfully produced, one of them having an in-line configuration with splices to Single-Mode Fibers (SMFs) on both ends.

Additionally, a previously unexplored solution in VOC optical fiber sensing was pre-

sented. Suspended-Core Fiber (SCF) tips were spliced to SMFs to create reflection-based sensing heads. By allowing VOCs to flow inside the holes of this special kind of MOF, it was possible to track their evaporation dynamics and distinguish the behaviour of acetone and isopropyl alcohol. This solution, based on the structural collapse of the SCF structure during the electric-arc fusion splicing step, avoids the need to fabricate lateral microcavities, a previous solution proposed in the literature, simplifying the sensor fabrication process.

As mentioned in the introduction, some results of this dissertation were disclosed to the scientific community through the participation in three conferences and also through the publication of an article in *Optics Letters*. Notwithstanding, further developments to the work here presented can be proposed:

Caterpillar Microstructured Fiber

- In order to enable the use of this fiber in other applications, it should be characterized in terms of its physical parameters, namely its response to temperature and strain. This step is already underway and preliminary results point to low temperature and strain sensitivities, ideal characteristics when low cross-sensitivity values are desirable.

- Alternative post-processing solutions can be pursued to try to optimize either the processing steps or the flow mechanics of the sensing head. As an example, a study could be performed on processing the fiber far from its tip in order to avoid structural collapse effects, enabling stronger splices to be performed.

- Taking into consideration the main purpose for its design and post-processing, tests should be done on the fiber's performance for fluid sensing. Initially, propagation properties with calibrated refractive index fluids can be done to assess the expected coupling between holes. Also, this fiber could be used in hot topics such as magnetic field sensing using advanced materials such as nanometric ferrofluidic suspensions.

Evaporation Monitoring with Suspended-Core Fibers

- Efforts should be put in a better modelling of the intensity dynamics by analyzing the influence of the other reflections identified. Since only the reflection at the splice was considered, it is expected that by contemplating other effects such as additional

reflections or splice losses, a better matching between model and experimental data would be achieved.

- In order to further evaluate this configuration's potential as a sensor, future work should include the study of a wider array of volatile compounds. By identifying the main signal components in the evaporation response, this simple sensing setup could be used to distinguish between different fluids and potentially recognize mixtures of volatile compounds.

The area of MOFs for fluid sensing is still in its early steps and much research is needed to enable the industrialization of many of the applications presented. One of the remaining difficulties is the high cost of fabricating specific MOF designs but even this is becoming a less critical step and some companies already offer the possibility of producing MOFs with particular details defined by the costumer. Another commonly discussed subject is the necessity to create microfluidic channels to bring fluids from the external environment close to a MOF's core. Many solutions are currently being researched and, in this regard, the present dissertation may have provided relevant contributions for the future, both with the FIB post-processing and the SCF-based sensing head.

Fluid sensing may prove useful not only for biochemical applications but also for physical measurements, such as magnetic field sensing using ferrofluids as the transduction medium, as previously mentioned. As such, the relevance of the present work is shown by the multitude of applications that can be envisaged in the field of sensing and measurement.

Bibliography

[1] G. P. Agrawal, *Fiber-Optic Communication Systems*, 3rd ed. New York: John Wiley & Sons, Inc., 2002.

[2] K. Kao and G. Hockham, "Dielectric-fibre surface waveguides for optical frequencies," *Proceedings of the Institution of Electrical Engineers*, vol. 113, no. 3, pp. 191–198, 1966.

[3] Nobelprize.org. (2013) "The Nobel Prize in Physics 2009". [Online] http://www.nobelprize.org/nobel_prizes/physics/laureates/2009/ [Accessed in 21 Dec 2013]

[4] B. Lee, "Review of the present status of optical fiber sensors," *Optical Fiber Technology*, vol. 9, no. 2, pp. 57–79, 2003.

[5] B. Culshaw, "Fiber optics in sensing and measurement," *IEEE Journal of Selected Topics in Quantum Electronics*, vol. 6, no. 6, pp. 1014–1021, 2000.

[6] *Fiber Optic Sensors: Global Markets.* BCC Research, 2011.

[7] *Fiber Optic Sensors Global Market Forecast & Analysis.* ElectroniCast Consultants, 2013.

[8] S. M. Klainer, "Fiber optic which is an inherent chemical sensor," 1989.

[9] W. R. Seitz, "Chemical Sensors Based on Fiber Optics," *Analytical Chemistry*, vol. 56, no. 1, pp. 16A–34A, 1984.

[10] X.-D. Wang and O. S. Wolfbeis, "Fiber-optic chemical sensors and biosensors (2008-2012)," *Analytical Chemistry*, vol. 85, no. 2, pp. 487–508, 2013.

[11] J. M. Fini, "Microstructure fibres for optical sensing in gases and liquids," *Measurement Science and Technology*, vol. 15, no. 6, pp. 1120–1128, 2004.

[12] B. Troia, A. Paolicelli, F. D. Leonardis, and V. M. N. Passaro, "Photonic Crystals for Optical Sensing : A Review," in *Advances in Photonic Crystals*, V. M. Passaro, Ed. InTech, 2013, pp. 241–295.

[13] B. H. Lee, Y. H. Kim, K. S. Park, J. B. Eom, M. J. Kim, B. S. Rho, and H. Y. Choi, "Interferometric fiber optic sensors," *Sensors*, vol. 12, no. 3, pp. 2467–86, 2012.

[14] W. Jin, J. Ju, H. L. Ho, Y. L. Hoo, and A. Zhang, "Photonic crystal fibers, devices, and applications," *Frontiers of Optoelectronics*, vol. 6, no. 1, pp. 3–24, 2013.

[15] C. M. B. Cordeiro, M. A. R. Franco, G. Chesini, E. C. S. Barretto, R. Lwin, C. H. Brito Cruz, and M. C. J. Large, "Microstructured-core optical fibre for evanescent sensing applications," *Optics Express*, vol. 14, no. 26, pp. 13 056–13 066, 2006.

[16] T. M. Monro, W. Belardi, K. Furusawa, J. C. Baggett, N. G. R. Broderick, and D. J. Richardson, "Sensing with microstructured optical fibres," *Measurement Science and Technology*, vol. 12, no. 7, pp. 854–858, 2001.

[17] O. Frazão, J. Santos, F. Araújo, and L. Ferreira, "Optical sensing with photonic crystal fibers," *Laser & Photonics Review*, vol. 2, no. 6, pp. 449–459, 2008.

[18] A. M. R. Pinto and M. Lopez-Amo, "Photonic Crystal Fibers for Sensing Applications," *Journal of Sensors*, vol. 2012, p. 598178, 2012.

[19] P. Jorge, M. A. Martins, T. Trindade, J. L. Santos, and F. Farahi, "Optical Fiber Sensing Using Quantum Dots," *Sensors*, vol. 7, no. 12, pp. 3489–3534, 2007.

[20] P. Bing, J. Yao, Y. Lu, and Z. Li, "A surface-plasmon-resonance sensor based on photonic-crystal-fiber with large size microfluidic channels," *Optica Applicata*, vol. XLII, no. 3, pp. 493–501, 2012.

[21] M. Born and E. Wolf, *Principles of Optics*, 6th ed. Pergamon Press Ltd., 1986.

[22] O. Frazão, "Sensores em Fibra Óptica Baseados em Interferometria e Efeitos Não-Lineares," Ph.D. dissertation, University of Porto, Porto, 2009.

[23] O. Frazão, P. Caldas, F. M. Araújo, L. A. Ferreira, and J. L. Santos, "Optical flowmeter using a modal interferometer based on a single nonadiabatic fiber taper," *Optics Letters*, vol. 32, no. 14, pp. 1974–6, 2007.

[24] J. Villatoro, V. P. Minkovich, V. Pruneri, and G. Badenes, "Simple all-microstructured-optical-fiber interferometer built via fusion splicing," *Optics Express*, vol. 15, no. 4, pp. 1491–6, 2007.

[25] R. A. Bergh, H. C. Lefevre, and H. J. Shaw, "All-single-mode fiber-optic gyroscope," *Optics Letters*, vol. 6, no. 4, pp. 198–200, 1981.

[26] J. Villatoro, V. Finazzi, G. Badenes, and V. Pruneri, "Highly Sensitive Sensors Based on Photonic Crystal Fiber Modal Interferometers," *Journal of Sensors*, p. 747803, 2009.

[27] S. H. Aref, R. Amezcua-Correa, J. P. Carvalho, O. Frazão, P. Caldas, J. L. Santos, F. M. Araújo, H. Latifi, F. Farahi, L. A. Ferreira, and J. C. Knight, "Modal interferometer based on hollow-core photonic crystal fiber for strain and temperature measurement," *Optics Express*, vol. 17, no. 21, pp. 18 669–75, 2009.

[28] P. Kaiser and H. W. Astle, "Low-Loss Single-Material Fibers Made From Pure Fused Silica," *Bell System Technical Journal*, vol. 53, no. 6, pp. 1021–1039, 1974.

[29] T. M. Monro and H. Ebendorff-Heidepriem, "Progress in Microstructured Optical Fibers," *Annual Review of Materials Research*, vol. 36, no. 1, pp. 467–495, 2006.

[30] J. C. Knight, T. A. Birks, P. S. J. Russell, and D. M. Atkin, "All-silica single-mode optical fiber with photonic crystal cladding," *Optics Letters*, vol. 21, no. 19, p. 1547, 1996.

[31] T. A. Birks, J. C. Knight, and P. Russell, "Endlessly single-mode photonic crystal fiber," *Optics Letters*, vol. 22, no. 13, pp. 961–963, 1997.

[32] R. F. Cregan, B. J. Mangan, J. C. Knight, T. A. Birks, P. S. J. Russell, P. J. Roberts, and D. C. Allan, "Single-Mode Photonic Band Gap Guidance of Light in Air," *Science*, vol. 285, no. 5433, pp. 1537–1539, 1999.

[33] O. Frazão, R. M. Silva, M. S. Ferreira, J. L. Santos, and A. B. Lobo Ribeiro, "Suspended-core fibers for sensing applications," *Photonic Sensors*, vol. 2, no. 2, pp. 118–126, 2012.

[34] K. Peters, "Polymer optical fiber sensors - a review," *Smart Materials and Structures*, vol. 20, no. 1, p. 013002, 2011.

[35] B. Eggleton, C. Kerbage, P. Westbrook, R. Windeler, and A. Hale, "Microstructured optical fiber devices," *Optics Express*, vol. 9, no. 13, pp. 698–713, 2001.

[36] J. C. Knight, "Photonic crystal fibres," *Nature*, vol. 424, no. 6950, pp. 847–851, 2003.

[37] P. Russell, "Photonic crystal fibers," *Science*, vol. 299, no. 5605, pp. 358–362, 2003.

[38] P. S. J. Russell, "Photonic-Crystal Fibers," *Journal of Lightwave Technology*, vol. 24, no. 12, pp. 4729–4749, 2006.

[39] R. Buczynski, "Photonic Crystal Fibers," *Acta Physica Polonica A*, vol. 106, no. 2, pp. 141–167, 2004.

[40] D. Richardson, F. Poletti, J. Leong, X. Feng, H. Heidepreim, V. Finazzi, K. Frampton, S. Asimakis, R. Moore, J. Baggett, J. Hayes, M. Petrovich, M. Tse, R. Amezcua, J. Price, N. Broderick, P. Petropoulos, and T. Monro, "Advances in microstructured fiber technology," in *Proceedings of 2005 IEEE/LEOS Workshop on Fibres and Optical Passive Components.* IEEE, 2005, pp. 1–9.

[41] O. Frazão, J. P. Carvalho, and H. M. Salgado, "Low-loss splice in a microstructured fibre using a conventional fusion splicer," *Microwave and Optical Technology Letters*, vol. 46, no. 2, pp. 172–174, 2005.

[42] H. Graebner. (2006) "Shargacucullia verbasci (Linneaeus, 1758), caterpillar". [Online] http://commons.wikimedia.org/wiki/File:Shargacucullia.verbasci.caterpillar.jpg [Accessed in 22 Jul 2014]

[43] S. Reyntjens and R. Puers, "A review of focused ion beam applications in microsystem technology," *Journal of Micromechanics and Microengineering*, vol. 11, no. 4, pp. 287–300, 2001.

[44] A. A. Tseng, "Recent developments in micromilling using focused ion beam technology," *Journal of Micromechanics and Microengineering*, vol. 14, no. 4, pp. R15–R34, 2004.

[45] *LYRA | FIB-SEM Brochure.* TESCAN, 2007.

[46] D. Iannuzzi, K. Heeck, M. Slaman, S. de Man, J. H. Rector, H. Schreuders, J. W. Berenschot, V. J. Gadgil, R. G. P. Sanders, M. C. Elwenspoek, and S. Deladi, "Fibre-top cantilevers: design, fabrication and applications," *Measurement Science and Technology*, vol. 18, no. 10, pp. 3247–3252, 2007.

[47] J.-L. Kou, S.-J. Qiu, F. Xu, Y.-Q. Lu, Y. Yuan, and G. Zhao, "Miniaturized Metal-Dielectric-Hybrid Fiber Tip Grating for Refractive Index Sensing," *IEEE Photonics Technology Letters*, vol. 23, no. 22, pp. 1712–1714, 2011.

[48] R. M. André, S. Pevec, M. Becker, J. Dellith, M. Rothhardt, M. B. Marques, D. Donlagic, H. Bartelt, and O. Frazão, "Focused ion beam post-processing of optical fiber Fabry-Perot cavities for sensing applications," *Optics Express*, vol. 22, no. 11, p. 13102, 2014.

[49] C. Martelli, P. Olivero, J. Canning, N. Groothoff, B. Gibson, and S. Huntington, "Micromachining structured optical fibers using focused ion beam milling," *Optics Letters*, vol. 32, no. 11, pp. 1575–7, 2007.

[50] C. Elosua, I. R. Matias, C. Bariain, and F. J. Arregui, "Volatile Organic Compound Optical Fiber Sensors: A Review," *Sensors*, vol. 6, no. 11, pp. 1440–1465, 2006.

[51] J. Villatoro, M. P. Kreuzer, R. Jha, V. P. Minkovich, V. Finazzi, G. Badenes, and V. Pruneri, "Photonic crystal fiber interferometer for chemical vapor detection with high sensitivity," *Optics Express*, vol. 17, no. 3, p. 1447, 2009.

[52] C. Liu and E. Bonaccurso, "Microcantilever sensors for monitoring the evaporation of microdrops of pure liquids and mixtures." *Review of Scientific Instruments*, vol. 81, no. 1, p. 013702, 2010.

[53] J. Wei, B. Shaw, and J. Xiao, "Transient measurements of the composition of evaporating droplets by fiber optic absorption spectroscopy," *Optics and Lasers in Engineering*, vol. 39, no. 1, pp. 91–108, 2003.

[54] E. Preter, R. A. Katims, V. Artel, C. N. Sukenik, D. Donlagic, and A. Zadok, "Monitoring and analysis of pendant droplets evaporation using bare and monolayer-

coated optical fiber facets," *Optical Materials Express*, vol. 4, no. 5, pp. 903–915, 2014.

[55] E. Preter, B. Preloznik, V. Artel, C. N. Sukenik, D. Donlagic, and A. Zadok, "Monitoring the evaporation of fluids from fiber-optic micro-cell cavities," *Sensors*, vol. 13, no. 11, pp. 15 261–15 273, 2013.

[56] T. M. Monro, S. Warren-Smith, E. P. Schartner, A. François, S. Heng, H. Ebendorff-Heidepriem, and S. Afshar, "Sensing with suspended-core optical fibers," *Optical Fiber Technology*, vol. 16, no. 6, pp. 343–356, 2010.

[57] A. S. Webb, F. Poletti, D. J. Richardson, and J. K. Sahu, "Suspended-core holey fiber for evanescent-field sensing," *Optical Engineering*, vol. 46, no. 1, p. 010503, 2007.

[58] T. Monro, D. Richardson, and P. Bennett, "Developing holey fibres for evanescent field devices," *Electronics Letters*, vol. 35, no. 14, pp. 1188–1189, 1999.

[59] T. G. Euser, J. S. Y. Chen, M. Scharrer, P. S. J. Russell, N. J. Farrer, and P. J. Sadler, "Quantitative broadband chemical sensing in air-suspended solid-core fibers," *Journal of Applied Physics*, vol. 103, no. 10, p. 103108, 2008.

[60] I. H. Malitson, "Interspecimen Comparison of the Refractive Index of Fused Silica," *Journal of the Optical Society of America*, vol. 55, no. 10, p. 1205, 1965.